Title

Zinc Finger MYND-Type Containing 8 (ZMYND8) Is Epigenetically Regulated in Mutant Isocitrate Dehydrogenase 1 (IDH1) Glioma to Promote Radioresistance.

Journal

Clinical Cancer Research, 29(9)

Authors

Carney, Stephen
Banerjee, Kaushik
Mujeeb, Anzar
et al.

Publication Date

2023-05-01

DOI

10.1158/1078-0432.CCR-22-1896

Peer reviewed

HHS Public Access

Author manuscript

Clin Cancer Res. Author manuscript; available in PMC 2023 November 01.

Published in final edited form as:

Clin Cancer Res. 2023 May 01; 29(9): 1763–1782. doi:10.1158/1078-0432.CCR-22-1896.

Zinc Finger MYND-Type Containing 8 (ZMYND8) is epigenetically regulated in mutant Isocitrate Dehydrogenase 1 (IDH1) glioma to promote radioresistance

Stephen V. Carney[1,2,3,4], **Kaushik Banerjee**[2,3,4], **Anzar Mujeeb**[2,3,4], **Brandon Zhu**[5], **Santiago Haase**[2,3,4], **Maria L. Varela**[2,3,4], **Padma Kadiyala**[6], **Claire E. Tronrud**[2], **Ziwen Zhu**[2,3,4], **Devarshi Mukherji**[7], **Preethi Gorla**[7], **Yilun Sun**[8], **Rebecca Tagett**[9], **Felipe J. Núñez**[2], **Maowu Luo**[10], **Weibo Luo**[10,11], **Mats Ljungman**[12,13], **Yayuan Liu**[14], **Ziyun Xia**[14], **Anna Schwendeman**[12], **Tingting Qin**[9], **Maureen A. Sartor**[9], **Joseph F. Costello**[15], **Daniel P. Cahill**[16], **Pedro R. Lowenstein**[1,2,4,6,17], **Maria G. Castro**[1,2,3,4,6,17]

[1]Cancer Biology Training Program, University of Michigan Medical School, Ann Arbor, MI 48109, USA.

[2]Department of Neurosurgery, University of Michigan Medical School, Ann Arbor, MI 48109, USA.

[3]Department of Cell and Developmental Biology, University of Michigan Medical School, Ann Arbor, MI 48109, USA.

[4]Rogel Cancer Center, University of Michigan Medical School, Ann Arbor, MI 48109, USA.

[5]Graduate Program in Biomedical Engineering, University of Michigan College of Engineering, Ann Arbor, MI, USA.

[6]Graduate Program in Immunology, University of Michigan Medical School, Ann Arbor, MI 48109, USA.

[7]Neuroscience, University of Michigan College of Literature, Science, the Arts (LSA), Ann Arbor, MI 48109, USA.

[8]Department of Radiation Oncology, University Hospitals/Case Western Reserve University, Cleveland, OH, USA.

[9]Department of Computational Medicine and Bioinformatics, University of Michigan, Ann Arbor, MI 48109, USA.

[10]Department of Pathology, UT Southwestern Medical Center, Dallas TX 75390, USA.

[11]Department of Pharmacology, UT Southwestern Medical Center, Dallas TX 75390, USA.

[12]Department of Radiation Oncology, University of Michigan Medical School, Ann Arbor, MI 48109, USA.

CORRESPONDING AUTHOR: Maria G. Castro, PhD, Room 4570B, MSRB II, 1150 W. Medical Center Dr., Ann Arbor, MI 48109-5689, Tel: 734-764-0850, Fax: 734-764-7051, mariacas@med.umich.edu.

CONFLICT OF INTEREST

The authors declare that there is no conflict of interest regarding the publication of this article.

[13]Department of Environmental Health Science, School of Public Health, University of Michigan, Ann Arbor, MI 48109, USA.

[14]Department of Pharmaceutical Sciences, University of Michigan, Ann Arbor, MI 48109, USA.

[15]Department of Neurological Surgery, University of California, San Francisco, California, 94143 USA.

[16]Department of Neurosurgery, Massachusetts General Hospital Cancer Center, Harvard Medical School, Boston Massachusetts, 02114, USA.

[17]Biosciences Initiative in Brain Cancer, University of Michigan Medical School, Ann Arbor, MI 48109, USA.

Abstract

Purpose: Mutant isocitrate dehydrogenase 1 (mIDH1) alters the epigenetic regulation of chromatin, leading to a hypermethylation phenotype in adult glioma. This work focuses on identifying gene targets epigenetically dysregulated by mIDH1 to confer therapeutic resistance to ionizing radiation (IR).

Experimental Design: We evaluated changes in the transcriptome and epigenome in a radioresistant mIDH1 patient-derived glioma cell culture (GCC) following treatment with an mIDH1 specific inhibitor AGI-5198. We identified Zinc Finger MYND-Type Containing 8 (ZMYND8) as potential target of mIDH1 reprogramming. We suppressed ZMYND8 expression by shRNA knockdown and genetic knockout (KO) in mIDH1 glioma cells then assessed cellular viability to IR. We assessed the sensitivity of mIDH1 GCCS to pharmacological inhibition of ZMYND8-interacting partners: HDAC, BRD4, and PARP.

Results: Inhibition of mIDH1 lead to an upregulation of gene networks involved in replication stress. We found that the expression of ZMYND8, a regulator of DNA damage response was decreased in three patient-derived mIDH1 GCCs after treatment with AGI-5198. Knockdown of ZMYND8 expression sensitized mIDH1 GCCs to radiotherapy marked by decreased cellular viability. Following IR, mIDH1 glioma cells with ZMYND8 knockout (KO) exhibit significant phosphorylation of ATM and sustained γH2AX activation. ZMYND8 KO mIDH1 GCCs were further responsive to IR when treated with either BRD4 or HDAC inhibitors. PARP inhibition further enhanced the efficacy of radiotherapy in ZMYND8 KO mIDH1 glioma cells.

Conclusions: These findings indicate the impact of ZMYND8 in the maintenance of genomic integrity and repair of IR-induced DNA damage in mIDH1 glioma.

Keywords

Epigenetic regulation; mutant IDH1 glioma; DNA repair; radiotherapy

Introduction

IDH-mutant gliomas account for roughly 80% of low-grade gliomas (1). The integration of histological classification with genomic analysis of concurrent mutations has defined the subtypes of IDH-mutant glioma as either astrocytoma (TP53 and ATRX inactivating

mutations), oligodendroglioma (TERT promoter amplification, 1p19q co-deletion), or recurrent glioblastoma (CDKN2A loss, CDK4 amplification) (2). The low grade mIDH1 tumors are slower growing, but highly infiltrative and arise predominantly within the frontal lobe (3). Patients harboring mutations in either IDH1 or IDH2 have a favorable prognosis as compared with high-grade wildtype-IDH glioma (4). Despite this finding, many IDH-mutant glioma patients treated with radiotherapy develop tumor progression and eventually succumb to the disease (5). The identification of molecular mechanisms that drive therapeutic response to IR in IDH1 glioma remains unexplored. In this respect, a recent report discusses recommendations for the implementation of radiation therapy taking into account the WHO 2021 classification of adult-type mutant IDH1 diffuse gliomas, which takes into account both molecular and histopathological features (6).

The characteristic heterozygous IDH1-R132H mutation produces an oncometablite 2-hydroxyglutarate (2HG) that impairs nuclear enzymes Jumonji-family of histone demethylases and TET2 methylcytosine dioxygenase inducing a IDH-specific hypermethylation phenotype (7,8). By reversing the epigenetic reprogramming elicited by IDH-mutations, we can elucidate how cellular pathways altered by mIDH1 support survival of tumor cells following radiation. In this study, we sought out to uncover gene targets that displayed alterations in chromatin regulation and gene expression following mIDH1 inhibition, and in turn discern their contribution to radioresistance. We have previously demonstrated that murine tumor neurospheres (NS) harboring mIDH1^{R132H} mutation display differential enrichment of H3K4me3 methylation at genomic regions associated with master regulators of the DNA Damage Response (DDR) (9). When we inhibited the DNA damage sensor ATM that initiates homologous recombination (HR) pathway or its downstream targets cell cycle checkpoint kinases 1 (Chk1) or 2 (Chk2), we observed enhanced radiosensitization of mIDH1-expressing GCCs. We also showed that pharmacological inhibition of mIDH1-R132H mutation in murine NS reduced mitotic cell proliferation and enhanced the release of Damage Associated Molecular Patterns (10). Additionally, administering a mIDH1 specific inhibitor (AGI-5198) in combination with ionizing radiation (IR) to mIDH1 tumor-bearing mice promoted tumor regression and the development of immunological memory (10).

We targeted mIDH1 using AGI-5198, which has been shown to decrease the production of 2HG and reverse histone hypermethylation (11). Herein, we evaluated changes in gene expression and epigenetic regulation in a radioresistant mIDH1 patient derived GCC following mIDH1 inhibition. We identified the significant downregulation of the chromatin reader protein, Zinc Finger MYND-Type Containing 8 (ZMYND8, also referred to as RACK7 and PRKCBP1). The connection between ZMYND8 and DNA repair was proposed based on its recruitment to nuclear sites of laser induced DNA damage (12). The presence of a bromodomain (BRD)-containing motif encoded within ZMYND8, was shown to recognize acetylated lysine residues, specifically H3K14ac and H4K16ac that are present on post-translational modified (PTM) histones (13). Recent high resolution crystal structure analysis of the ZMYND8 protein, explored the putative chromatin reader function of adjacent domains to bind specific histone marks. The plant homeodomain (PHD) recognizes singly methylated lysines (H3K4me1), while the hydrophobic Pro-Trp-Trp-Pro (PWWP) domain recognizes H3K36me2 (13). These effector domains support early findings that ZMYND8

accumulated at actively transcribed regions where double stranded breaks (DSB) occurred (12).

During DNA repair, there are dynamic changes to chromatin organization, which allows for the recruitment of DDR proteins. Sites of DNA damage display reductions in active histone mark H3K4me3 signal that co-localizes with hallmark DNA damage markers like γ-H2AX (14). The recruitment of ZMYND8 to regions of DNA damage is dependent on H3K4me2/3 demethylase KDM5A, proposing a role of transcriptional repression in DNA repair mediated by HR mechanisms (14). ZMYND8 interacts with several subunits of the Nucleosome Remodeling and Histone Deacetylase (NuRD) complex: Chromodomain Helicase DNA Binding Protein 4 (CHD4), histone deacetylases 1 and 2 (HDAC1/2) and GATA Zinc Finger Domain Containing 2A (GATAD2A) to facilitate HR-dependent DNA repair (15). This process is shown to be regulated by Poly ADP-ribose polymerase (PARP) dependent recruitment to regions of DNA damage to facilitate a cascade of transcriptional repression (15). Previous work has shown that ZMYND8 associates with activator complexes like pTEF-b and BRD4 to regulate gene expression at enhancers and active gene regions (16,17). Within the realm of tumor biology, ZMYND8 has been linked to the regulation of cancer-specific programs in colorectal, prostate, breast, H3.3G34R mutant glioma, acute myeloid leukemia, renal cell carcinoma, non-small cell lung cancer (NSCLC), nuclear protein in testis (NUT) carcinoma and hepatocellular carcinoma (18–26).

Herein, we explore resistance mechanisms reinforced by IDH1 reprogramming that allows tumor cells to survive radiotherapy. We have previously shown, mIDH1 GCCs are more resistant to radiotherapy and that inhibition of mIDH1 using AGI-5198 enhances cellular death following radiation (9,10). In this study, we utilize three mIDH1 GCCs and our genetically engineered tumor NS that endogenously express IDH1-R132H mutation in the context of ATRX and TP53 loss (NPAI). When we reverse IDH1 reprogramming by treating a human mIDH1 GCC with AGI-5198, we observe significant reduction in ZMYND8 expression and induction of replication stress genes. Mouse mIDH1 glioma cells express higher ZMYND8 transcripts and display elevated H3K4me3 methylation at the promoter region of ZMYND8 when compared to wildtype IDH1 (wtIDH1) mouse glioma cells. Knocking out ZMYND8 in two mIDH1 patient derived GCC and our genetically engineered mIDH1 mouse tumor neurospheres sensitizes the glioma cells to radiation. Our findings demonstrate that loss of ZMYND8 in mIDH1 GCCs induces greater DNA damage based on higher levels of ATM and γH2AX phosphorylation. This decrease in cellular viability of ZMYND8 KO mIDH1 GCC could be the result of cell cycle arrest induced by p-Chk1 activation. To date, ZMYND8 has been implicated in driving cancer-specific programs mediated by its function at enhancers and through its role in PARP-dependent transcriptional repression. Our data supports the clinical evaluation of PARP, BRD4, or HDAC inhibition to interfere with ZMYND8 mediated repair mechanisms and improve the therapeutic efficacy of irradiation.

Materials and Methods

Cell Culture

Human SF10602 cells (27) were grown in NeuroCult NS-A Basal Medium supplemented with 100units/mL antibiotic-antimycotic, 10mL B-27 without vitamin A, 5mL N-2, 100μg/ml Normocin, 20ng/mL FGF, 20ng/mL EGF, and 20ng/mL PDGF-AA. Human MGG119 (28) and LC1035 GCCs were grown in Neurobasal media supplemented with 100units/mL antibiotic-antimycotic,10mL B-27, N-2, 100μg/ml normocin, 20ng/mL FGF, 20ng/mL EGF, and 20ng/mL of PDGF-AA. Mouse mIDH1 NS were grown in DMEM-F12 media supplemented with 100units/mL antibiotic-antimycotic, B27, N2, 100μg/mL normocin, 10ng/mL FGF and 10ng/mL EGF. Stable generation of ZMYND8 KO glioma cells were maintained in culture with 10ug/mL puromycin. Glioma cells were dissociated using StemPro Accutase solution and passaged every 4 days for mouse NS and weekly for human glioma cells. Human glioma cells were shared through the following collaborations: Dr. Daniel Cahill laboratory, Harvard Medical School (MGG119) and Dr. Joseph Costello laboratory, UCSF (SF10602). LC1035 were generated in our laboratory through our collaboration with the University of Michigan's Department of Neurosurgery.

Detection of 2HG in conditioned media of mIDH1 GCC following mIDH1 inhibition

The conditioned media was collected from three human mIDH1 GCCs that were untreated, treated with either vehicle (DMSO) or mIDH1 inhibitor (AGI-5198, DS-1001b) for 1 week. Samples were stored at −80°C prior to assessment by liquid chromatography-mass spectrometry (LC-MS). Conditioned media (50 μL) was mixed with 10 μL of internal standard spike-in solution 10 μg/mL of 2-HG-D3 (Sigma-Aldrich) and was homogenized in 1 mL of 80% methanol in aqueous solution. The homogenate was centrifuged at 12000 rpm for 10 min at 4°C, and the supernatant was collected and dried under a stream of nitrogen at 37°C. The extracted sample was then combined with 160 μL of N-(p-toluenesulfonyl)-L-phenylalanyl chloride (TSPC, 2.5 mM in acetonitrile) and 2 μL of pyridine was added and incubated at 37°C for 20 min to derivatize D-2HG. After derivatization the mixture was dried with nitrogen at 37°C and reconstituted in 100 μL of 50% acetonitrile in aqueous solution. The samples were then centrifuged at 12000 RPM for 10 min and the supernatant was collected for quantification.

The quantification of 10μl of derivatized 2-HG was carried out using ultra performance (UP) UPLC-MS (Waters ACQUITY system). The mobile phase consisted of deionized water containing 0.1% formic acid (A) and acetonitrile/methanol (1:1, v/v) containing 0.1% formic acid (B). The gradient started from 70% A and maintained for 1 min, changed to 30% A over 3 min and maintained for 2 min, and finally changed back to 70% A over 0.5 min and held for 1.5 min. The flow rate was 0.5 mL/min, and column temperature was set at 40 °C. The analysis was performed on a Waters ACQUITY UPLC HSS T3 column (1.8 μm, 3.0 × 75 mm) with mass detection at 448.17 (−) for derivatized 2-HG, and at 451.19 (−) for derivatized 2-HG-D3. The 2HG concentration measurements presented in Figure 1B can be found in Supplementary Table S2.

RNA-sequencing (RNA-seq)

Bulk RNA-Sequencing was performed in collaboration with the University of Michigan (UM) Advanced Genomics Core (AGC), using the NovaSeq-6000 platform for 150-base paired-end reads. Total RNA was isolated from patient-derived mIDH1 GCC SF10602 untreated and AGI-5198-treated using the RNeasy Plus Mini Kit and 100ng of RNA was submitted to the UM AGC. RNA quality was assessed using the TapeStation, samples with an RIN (RNA Integrity Number) of 8 or greater were prepared using Illumina TruSeq mRNA Sample Prep Kit v2. cDNA Library preparation was performed by UM DSC using a ribo-depleted RNA protocol method. Results are from 3 technical replicates per condition; SF10602 untreated or treated with mIDH1 inhibitor AGI-5198 for 1 week. Information pertaining to the number of aligned reads utilized for our RNA-seq analysis can be found in Supplementary Table 1. RNA-Seq dataset generated in this study have been deposited at the NCBI's Gene Expression Omnibus (GEO) with identifier GSE220716.

Bioinformatics analysis of RNA-seq for differential expression

Illumina NovaSeq read files were downloaded to the Sequencing Core storage and concatenated into a single fastq file for each sample. In collaboration with the UM Bioinformatics Core, we checked the quality of the raw reads data for each sample using FastQC (version v0.11.3) to identify features within the data that may indicate quality issues (e.g. low quality scores, over-represented sequences, inappropriate GC content). We aligned reads to the reference genome (UCSC hg19) using Bowtie 2 (RRID:SCR_016368). Expression quantitation was performed with HTSeq (RRID:SCR_005514), set to count non-ambiguously mapped reads only. Data were pre-filtered to remove genes with 0 counts in all samples. Normalization and differential expression was performed with DESeq (RRID:SCR_000154) which uses a negative binomial generalized linear model. Resultant p-values were corrected for multiple hypotheses using the Benjamini-Hochberg False Discovery Rate (FDR). Genes and transcripts were identified as differentially expressed based on FDR ≤ 0.05, and fold change $\geq \pm 1.5$. The volcano plot was produced using an R base package and encompasses all genes identified by our RNA-seq analysis.

GSEA Enrichment Map and Gene Ontology (GO) Analysis

All 1335 differentially expressed genes between SF10602 treated with AGI-5198 (mIDH1 specific inhibitor) vs. untreated SF10602 were exported to a table with their gene names in the first column and log2-fold change values in the second column, sorted to produce gene ranks. The rank file was used as input to the GSEA (Gene Set Enrichment Analysis), downloaded from the Broad Institute (http://www.gsea-msigdb.org/gsea/login.jsp) (SeqGSEA, RRID:SCR_005724). The Broad Institute MSigDB includes the complete Gene Ontology (GO) (c5.all.v7.5.1.symbols.gmt), which we used as the input Knowledgebase. GSEA was run with 2000 permutations and gene set size range restricted to between 0 and 200 genes. An enrichment map was generated using the Cytoscape Platform (v3.9.1), which requires the rank and gmt file along with the positive/negative GSEA results. Each circle represents an individual GO term, and the size of the circle represents the number of genes within that set. The color of the circle signifies the directionality of expression in the mIDH1 inhibitor treated (AGI-5198) compared to untreated, where red is upregulated in AGI-5198-

treated compared to untreated while blue is downregulated. We included all differentially enriched GO pathways that had a p-value<0.01 and FDR<0.05 as shown in Supplementary Figure S1. The enrichment score plots for Replication Fork, DNA Replication Initiation and Nuclear Replication Fork are shown in Figure 1E, which are images provides in the GSEA Pre-ranking report.

ChIP-seq

SF10602 were cultured in the presence of 5μM AGI-5198 (mIDH1 inhibitor) or the vehicle (DMSO) for 10 days prior to isolation for chromatin immunoprecipitation (ChIP). Modifications to laboratory native ChIP-seq protocol as previously described previously (29,30) were as follows: 1.) increased cell number per histone mark IP from $1x10^6$ to $3x10^6$, 2.) increased histone mark antibody concentration to 2μg, 3.) extended Dynabead A/G incubation to 6hrs, and 4.) doubled Dynabead A/G concentration. ChIP-Seq dataset generated in this study have been deposited at the NCBI's Gene Expression Omnibus (GEO) with identifier GSE220715.

Lentiviral particle generation

Second generation lentiviral particles were packaged using HEK293T cells, which were seeded at 5 million cells and incubated with plasmid transfection mix containing 80μl of jetPRIME solution, 2 mL of PEG, envelope (10μg), package (15μg) and lentiCRISPR-V2-ZMYND8 (20μg) plasmid provided by Dr. Weibo Lou at UTSW. (Wang et al. 2021 Cancer Research) Lentiviral particles were purified from conditioned media by centrifuging at 30,000 rpm for 2hrs. After ultra-centrifugation, the concentrated lentiviral particles were resuspended in 1 mL of ice-cold PBS under gentle agitation 25rpm at 4°C for 1hr. Lentiviral particle solution was aliquoted into cryo-safe microcentrifuge tubes and stored at −80°C for later use.

Intracranial mIDH1 glioma model

All animal studies were conducted according to guidelines approved by the IACUC of the University of Michigan (protocols PRO00009578 and PRO00009546). All animals were housed in an AAALAC-accredited animal facility and were monitored daily. Studies did not discriminate by sex; both male and females were used. The strains of mice used in the study were C57BL/6 (the Jackson Laboratory, strain no. 000664) and CD8-KO (the Jackson Laboratory, strain no. B6.129S2-Cd8atm1Mak/J, stock no. 002665).

Our laboratory has modelled mIDH1 low grade glioma by integrating oncogenic plasmid DNA into the neural stem cells present within the developing brain of post-natal mice utilizing the sleeping beauty (SB) transposon system. The mIDH1 glioma cells endogenous express IDH1-R132H along with genetic lesions that drive oncogenesis through $NRAS^{G12V}$ and simulate tumor suppressor loss by ATRX and TP53 short hairpin knockdown. Tumor NS were derived from endogenous mIDH1 tumors that were adapted to *in vitro* culture and could be reimplanted into immunocompetent C57BL6 (The Jackson Laboratory, C57BL/6J Strain# 000664) mice for preclinical experiments in this study. Intracranial surgeries were performed by stereotactically injecting 50,000 mIDH1 NS into the right striatum using a

22-gauge Hamilton syringe with the following coordinates: 1.0 mm anterior, 2.5mm lateral and 3.0mm deep from the bregma suture line.

Generation of human and mouse ZMYND8 KO glioma cells

Human mIDH1 primary glioma cell cultures SF10602 and MGG119 were seeded at $2x10^5$ cells per well of laminin coated 6-well plate. The following day, cell culture media was removed, and cells were incubated directly with lentiviral particles for 10mins. Media was changed after 3 days of lentiviral transfection and cells were expanded for another week prior to puromycin selection. Loss of ZMYND8 expression was confirmed by WB after 5 days of puromycin selection.

Embedding mIDH1 GCC NS for Immunohistochemistry

Following 1 week treatment with vehicle (DMSO) or 5μM mIDH1 inhibitor (AGI-5198), mIDH1 NS were transferred to 15 mL conical and allowed to settle by gravity. The supernatant was removed by manual pipetting and mIDH1 NS were suspended gently in 4% PFA for overnight incubation to fix and retain neurosphere morphology. The next day mIDH1 NS were washed thrice in PBS buffer. Autoclaved 4% low-melting agarose was cooled to 43°F on bead bath. In order to embed mIDH1 NS in agarose, cells were transferred to 1.5mL microcentrifuge tube and 200μl of agarose was added over top of the NS. A wooden skewer was used to evenly distribute mIDH1 NS before immediately transferring to ice. Agarose cone containing mIDH1 NS was removed and processed at Histology core for paraffin sectioning. Representative sections of mIDH1 NS were made at 5μm thickness and transferred to microscope slides. Immunohistochemistry (IHC) was performed by heating slides to 60°C for 20mins to assist in remove of paraffin. NS slides were deparaffinized and rehydrated. Permeabilization of NS was performed using TBS-0.025% Triton-X (TBS-TX) for 20 min. Antigen retrieval was performed at 96°C with citrate buffer (10mM sodium citrate, 0.05% Tween-20, pH 6) for an additional 20 min. Once cooled to room temperature (RT), sections were outlined with hydrophobic barrier pen, washed thrice (3min washes) with TBS-TX and blocked with 10% horse serum (HS) for 1hr at RT. IHC sections were incubated in primary antibody ZMYND8 (1:2000) (Bethyl Laboratories, Cat.# A302–089A) diluted in 5% HS TBS-TX overnight in 4°C cold room. The following day, sections were washed with TBS and incubated with biotinylated secondary antibody goat anti-rabbit (1:1000) (Dako, Agilent Technologies, goat anti-rabbit 1:4000 (Cat# P0448) for 1h at RT. Next, slides were washed thrice in TBS and incubated with Vectastain ABC reagent for 30mins covered by aluminum foil. Following TBS wash, slides were developed using Betazoid DAB Chromogen kit (Biocare BDB2004) for 1–2mins at RT.

In vitro Dose-Response and evaluation of radiosensitivity using PARP inhibitor

To assess the susceptibility of both ZMYND8 WT and ZMYND8 KO generated in mouse mIDH1 NS and human mIDH1GCCs to PARP inhibitor (PARPi), we used Pamiparib (BGB-290) (SelleckChem, Cat# S8592), a PARPi for our study. Herein, both the cells were plated at a density of 1500 cells per well in 96-well plates (Fisher, 12–566-00) 24h prior to treatment. We used 5 wells per inhibitor dose evaluated for each cell type. We evaluated 8 concentrations of inhibitor in serial dilutions (e.g., 1μM, 3μM, 10μM, 30μM, 50μM, 100μM) and were added to each well for each dilution evaluated. Cells were then

incubated for 3 days and viability was assessed using CellTiter-Glo assay (Promega, Cat# G7572) following manufacturer's protocol. Moveover to assess the radiosensitization, cells were then incubated with either Pamiparib alone or in combination with radiation at their respective IC_{50} doses for 72h in triplicate wells per condition. Cells were pre-treated with PARPi 2h prior to irradiation with 6Gy and 20Gy of radiation for mouse neurospheres and human glioma cells respectively. Resulting luminescence was read with the Enspire Multimodal Plate Reader (Perkin Elmer). Data was represented graphically using the GraphPad Prism 7 (RRID:SCR_002798) using sigmoidal regression model which allows the determination of IC_{50} values and statistical significance was determined by one-way ANOVA followed by Tukey's test for multiple comparisons.

Western blot and radiation sensitivity *in vitro*

Mouse NS (NPA-C54B: wt-IDH1, NPAI: mIDH1) and human mIDH1 GCCs (SF10602 and MGG119) were seeded at density of 5.0 x 10^6 cells into 75-cm2 flasks containing NSC media. After 24 hours, mouse NS and human GCCs were treated with 5Gy and 20Gy radiation, respectively. After an additional 48 hours, cell lysates were prepared by incubating glioma cells with RIPA lysis buffer (MilliporeSigma, Cat# R0278) and 1X Halt™ protease and Phosphatase inhibitor cocktail, EDTA-free (100X) (Thermo Scientific, Cat# 78441) on ice for 15 minutes. Resulting cell lysates were centrifuged at 14000 RPM at 4°C for 15 minutes and supernatants were collected to determine protein concentration in comparison to standard bovine serum albumin (BSA) protein concentrations through bicinchoninic acid assay (BCA) (Pierce, 23227). For electrophoretic separation of proteins, 20 μg of total protein were resuspended in loading buffer (10% sodium dodecyl sulfate, 20% glycerol, and 0.1% bromophenol blue) and samples were heated at 95°C for 5mins to denature protein and later loaded onto a 4–12% Bis-Tris gel (Thermo Fisher Scientific, NuPAGE, NP0322BOX). Proteins from the gel were transferred to 0.2 μm nitrocellulose membrane (Bio-Rad, Cat# 1620112) and blocked with 5% bovine serum albumin (BSA) in TBS-0.1% Tween-20. After blocking, membranes were incubated with primary anti-phospho γH2AX (1:1000) (Cell Signaling Technologies, Cat# 9718S), anti-γH2AX (1:1000) (Cell Signaling Technologies, Cat# 2595S), primary antibody ZMYND8 (1:2000) (Bethyl Laboratories, Cat# A302–089A), primary antibody TIMELESS (1:1000) (Bethyl Laboratories, Cat.# A300–960A), primary antibody PCNA (1:1000) (Cell Signaling Technologies, Cat# 2586T), primary antibody TREX1 (1:1000) (Abcam, Cat# ab185228), primary antibody BRD4 (1:1000) (Cell Signaling Technology, Cat# 83375B), primary antibody HDAC1 (1:1000) (Cell Signaling Technology, Cat# 2062S), primary antibody HDAC2 (1:1000) (Cell Signaling Technology, Cat# 57156S), Vinculin (1:3000) (Thermo Fisher Scientific, Cat# 7000062) or β-tubulin antibodies (1:4000) (Sigma-Aldrich, Cat# A1978) overnight at 4°C. The next day, blots were washed with TBS-0.1% tween-20 and incubated with secondary (1:4000) antibodies [Dako, Agilent Technologies, goat anti-rabbit 1:4000 (Cat# P0448), rabbit anti-mouse 1:4000 (Cat# P0260)] for one hour at room temperature. Blots were washed several times again with TBS-0.1% tween-2.0 Enhanced chemiluminescence reagents were used to detect the signals following the manufacturer's instructions (SuperSignal West Femto, Thermo Fisher Scientific, Cat# 34095) and visualized under Bio-Rad gel imaging software. Band intensities were quantified using ImageJ (RRID:SCR_003070).

Tumor implantation and inhibition of DNA damage response *in vivo*

NPAI ZMYND8-WT GCCs (50,000 cells) were implanted in immunocompetent C57BL6 (The Jackson Laboratory, C57BL/6J Strain# 000664) mice. Mice were anesthetized using ketamine (75mg/kg, I.P) and dexmedetomidine (0.5mg/kg, I.P) before stereotactic implantation with cells in the right striatum. The coordinates for implantation were 1.0 mm anterior and 2.0 mm lateral from the bregma, and 3.5 mm ventral from the dura. Neurospheres were injected at a rate of 1 μL/min. Mice were given a combination of buprenorphine (0.1mg/kg, S.C) and carprofen (5mg/kg, S.C) for analgesia. Tumor burden was confirmed based on IVIS bioluminescence signal at 10 days post-implantation (dpi), and the mice were divided into 4 groups: i. Saline; ii. Pamiparib injected (1mg/mL); iii. IR treated; and iv. Pamiparib+IR. Mice were administered with 10 mg/Kg of Pamiparib, dissolved in 10% (2-hydroxypropyl)- β-cyclodextrin (Sigma Aldrich, Cat# H107–5G), and injected in a volume of 200 uL, 5 days per week for two weeks. Mice were lightly anesthetized with isoflurane and placed under a copper Orthovoltage source, with the irradiation beam directed to the brain, while the body was shielded by iron collimators. A dose of 2 Gy per irradiation session was given 5 days per week for two weeks, for a total of 20 Gy. Irradiation treatment was given to the mice at the University of Michigan Radiation Oncology Core.

Data Availability

There are no limitations on data availability. The ChIP-Seq dataset generated in this study can be acquired through NCBI's Gene Expression Omnibus (GEO) with identifier GSE220715. The RNA-Seq dataset generated in this study can be acquired through NCBI's Gene Expression Omnibus (GEO) with identifier GSE220716. All other data generated within this study are available via the supplementary data files; cells and plasmids will be freely distributed upon request from the corresponding author, Maria G Castro.

Results

Inhibition of mIDH1 by AGI-5198 leads to the upregulation of replication associated pathways

In this study, we sought to determine radioresistance mechanisms in IDH-mutant gliomas that contribute to glioma cell survival in response to radiotherapy. We utilized a radioresistant patient-derived glioma cell culture SF10602, which retained the endogenous mutations in IDH1-R132H, ATRX and TP53 after adaptation to *in vitro* culture (27). In order to identify pathways altered by mIDH1 inhibition in SF10602, we performed a transcriptomic (RNA-seq) and epigenomic (ChIP-seq) screen (Fig. 1A) by administering 5μM AGI-5198 every 2 days for 1 week. It has been shown that 2HG is released within the conditioned media of mIDH1 GCC maintained *in vitro* (31). To confirm that our mIDH1 inhibitor treatment schedule inhibited 2HG production, we collected the conditioned media from untreated and AGI-5198 treated mIDH1 GCCs to analyze the presence of 2HG by liquid chromatogram and mass-spectrometry (LCMS). We observed a significant reduction of 2HG levels (Fig. 1B) in three mIDH1 GCCs SF10602, LC1035 and MGG119 following treatment with AGI-5198 or another mIDH1 inhibitor DS-1001b currently in phase II clinical trials (NCT04458272) as compared to the vehicle control DMSO. Inhibition

of mIDH1 by AGI-5198 resulted in dynamic changes in transcriptional regulation (Fig. 1C), where we observed 1,335 differentially expressed genes consisting of 498 upregulated and 839 downregulated genes based on a log2 fold-change (log_2FC) cut-off greater than ±0.6. We performed a gene set enrichment analysis (GSEA) of these differentially genes altered by mIDH1 inhibition to uncover pathways dependent upon mIDH1 reprogramming (Supplementary Fig. S1). Of the down-regulated gene ontologies (GO) associated with ZMYND8 were involved in transcription factor binding and cellular movement (Fig. 1D). We observe an upregulation of GOs associated with replication (Fig. 1E) specifically Replication Fork (GO:0005657), DNA Replication Initiation (GO:0006270) and Nuclear Replication Fork (GO:0043596). Many of the genes shared across the replication associated GOs have roles in regulating replication stress facilitated by the stalling and restart of replication forks (Fig. 1E). In addition, the genes that were upregulated following mIDH1 inhibitor treatment function as part of the core replisome or have been associated with responding to replicative stress. This data suggests that blocking 2HG production in mIDH1 GCCs using AGI-5198 induces replicative stress.

Epigenetic Changes following mIDH1 inhibition suggests activation of replication stress

When cells divide, there must be a strict coordination between transcription and replication to ensure the maintenance of genomic stability. This tightly regulated process is disrupted in cancer cells as a result of oncogene activation (32). The destabilization of replication forks or collision events between mediators of transcription and replication can generate DSB. To address replication stress, cells express proteins involved in cell cycle arrest, replication fork restart, and DNA repair to resolve damaged DNA regions (32). In order to translate the elevated expression of replication stress genes to their regulation at the chromatin level, we performed chromatin immunoprecipitation and deep sequencing (ChIP-seq) for histone marks associated with active transcription (H3K4me3, H3K36me3), enhancers (H3K4me1, H3K27ac) and transcriptional repression (H3K27me3) in SF10602 in the presence of AGI-5198 (Fig. 2A).

We focused on mediators of the HR pathway, we found ZMYND8 to one of the most significantly downregulated genes following the treatment of SF10602 with AGI-5198 (Fig. 1C). The chromatin reader ZMYND8 has been shown to be recruited to DSB at actively transcribed regions (12). Depletion of ZMYND8 by siRNA or knockout impaired the recruitment of RAD51 foci at sites of DNA damage (12,15). We observed a significant loss of the active histone mark H3K4me3 at three distinct regions (I, II, III) near the promoter of ZMYND8 following mIDH1 inhibition by AGI-5198 (Fig. 2B).

To determine if the upregulation of ZMYND8 was dependent on mIDH1 expression, we assessed nascent transcription by bromouridine sequencing (Bru-seq) within our genetically engineered mouse glioma model comparing mouse tumor NS clones expressing either wtIDH1 (NPA) or mIDH1 (NPAI) (Supplementary Fig. S2A). Mouse mIDH1 NS displayed an enhanced transcription rate for *ZMYND8* (1.27-fold), along with HR proteins mediators *RAD50* (1.78-fold), *FANCA* (1.63-fold) and *RAD51* (1.30-fold) compared to the wtIDH1 NS (Supplementary Fig. S2B). To determine whether there were differences in the epigenetic regulation of ZMYND8 in the mIDH1 NS compared to wtIDH1 NS, we

analyzed H3K4me3 enrichment at the ZMYND8 locus. We found five PePr differential enriched peaks (i-v) that showed significantly higher H3K4me3 enrichment corresponding to ZMYND8 promoter regions across the mIDH1 NS (NPAI C1, C2, C3) versus wtIDH1 NS (NPA C54A, C54B, C2) clones (Supplementary Fig. S2C). These findings suggest that mIDH1 epigenetically regulates ZMYND8 by increasing H3K4me3 deposition at the promoter leading to enhanced transcription.

Next, we investigated the epigenetic changes that occurred at genes associated with replication stress. We observed elevated H3K27ac deposition at the promoter regions of genes associated with replication following AGI-5198 treatment (Fig. 2C). The progression of replication forks is facilitated by the unwinding of DNA by the replisome, which is comprised of claspin (CLSPN) and Timeless (TIMELESS) and the tethering of DNA polymerase by proliferating cell nuclear antigen (PCNA) (33). Methyl methanesulfonate-sensitivity protein 22-like (MMS22L) functions in a complex with Tonsoku Like (TONSL), where it has been shown to be required for replication fork stability by binding newly incorporated histones and aiding in RAD51 loading (34). The flap endonuclease 1 (FEN1) resolves nicks in DNA that arise during replication (35). The DEAD/H-BOX Helicase 11 (DDX11) facilitates the progression of replication forks by unwinding G-quadraplexes (36). The endonuclease V (EXO5) supports replication fork restart and EXO5 expression is correlated with higher mutational burden in solid tumors (37). Three Prime Repair Exonuclease 1 (TREX1) degrades cytosolic DNA released from the nucleus as a result of chromosomally unstable cells (38). These data suggest that mIDH1 inhibition enhances the activation of replication stress genes marked by elevated deposition of regulatory histone mark H3K27ac at the promoter regions.

When we examined the chromatin regions of genes downregulated with AGI-5198 treatment and were associated with replication, we observed loss of H3K36me3 deposition throughout the promoter and gene body (Fig. 2D). BTB Domain and CNC Homolog 1 (BACH1) has a role in activating ATR-dependent Chk1 phosphorylation (39). Egl-9 Family Hypoxia Inducible Factor 3 (EGLN3) drives ATR-mediated repair under hypoxic conditions (40). TP63 regulates transcription at tissue-specific enhancers and conditional ablation of p63 lead to apoptosis of adult neural precursors cells in postnatal mice (41). These data suggest transcriptional suppression of proteins involved in ATR activation following mIDH1 inhibition.

Inhibiting mIDH1 suppresses expression of ZMYND8

Epigenetic regulation of a gene is defined by the patterns of specific histone modifications at the genomic locus and correlates with chromatin accessibility and gene expression. H3K4me3 is enriched at sites of poised and actively transcribed regions, which highlights the activity of genes that govern cell-specific networks. We sought to determine if the significant reduction of H3K4me3 at the ZMYND8 promoter following AGI-5198 treatment in the SF10602 would lead to a decrease in protein expression. We first determined the concentration of 2-hydroxyglutarate (2-HG) present within the conditioned media over a week following AGI 5198 treatment. We found decreased amounts of 2-HG within the conditioned media of SF10602 mIDH1 glioma cells treated with AGI-5198 compared to

SF10602 mIDH1 glioma cells treated with the vehicle DMSO (Supplementary Fig. 3). We included two additional human mIDH1 GCCs (MGG119, LC1035) to evaluate if the inhibition of mIDH1 lead to a decrease in ZMYND8 gene expression across mIDH1 GCCs derived from separate patients. We performed western blotting (WB) for ZMYND8 in three human mIDH1 GCCs treated with AGI-5198 (Fig. 3A). We observed a significant reduction of ZMYND8 protein expression in the MGG119 ($p<0.0001$), SF10602 ($p<0.0001$) and LC1035 ($p<0.0001$) following AGI-5198 treatment (Fig. 3B). To confirm that this modulation of ZMYND8 protein expression was consistent with mIDH1 inhibition, we treated the human mIDH1 GCCs with DS-1001b (Fig. 3C). We observed a significant reduction of ZMYND8 expression in the MGG119 ($p < 0.05$), SF10602 ($p < 0.0001$) and LC1035 ($p < 0.01$) after DS-1001b treatment (Fig. 3D). Considering that western blots are representative of the bulk sample, we performed immunohistochemistry for ZMYND8 on paraffin-embedded human mIDH1 NS pre-treated with AGI-5198. This allowed us to determine the impact of mIDH1 inhibition on ZMYND8 expression at the individual cell level (Fig. 3E). We analyzed the nuclear IHC staining of ZMYND8 using Quantitative Pathology & Bioimage Analysis (QuPath) to define the number of ZMYND8 positive cells per frame (Supplementary Fig. S4A). We observed a significant reduction in the percentage of ZMYND8 positive nuclei in the SF10602 ($p< 0.001$) and LC1035 ($p < 0.0001$) pre-treated with AGI-5198 compared the DMSO treated (Fig. 3F). Pre-treatment of LC1035 with DS-1001b prompted a similar reduction in the percentage of ZMYND8 positive nuclei (Supplementary Fig. S4B). These data demonstrate that mIDH1 epigenetically regulates ZMYND8 protein expression, which is suppressed by mIDH1 inhibition.

The reproducible reduction of ZMYND8 protein expression following mIDH1 inhibition led us to explore whether the decrease in ZMYND8 coincided with changes in proteins involved in replication stress (Fig. 3G). To address this, we collected protein from SF10602 that were untreated, treated with vehicle (DMSO) or 5μM AGI-5198 every 2 days for 1 week. First, we investigated the protein expression of TREX1, an exonuclease that sequesters ssDNA fragments generated from aberrant replication and has been shown to be recruited to stalled replication forks (Fig. 3G) (42). We observed a significant increase in TREX1 protein expression in SF10602 treated with AGI-5198 when compared to DMSO treated cells ($p < 0.05$) (Fig. 3H). Next, we evaluated the expression of PCNA and TIMELESS, which are known to be co-expressed during S phase (Fig. 3I) (43). We observed a significant increase in PCNA protein expression in SF10602 treated with AGI-5198 ($p < 0.01$) compared to untreated cells, and a modest increase ($p < 0.05$) in DMSO-treated cells (Fig. 3J). Similarly, we found TIMELESS to be significantly increased following AGI-5198 treatment ($p < 0.001$) compared to untreated SF10602. In order to maintain the structural stability of stalled replication forks, Timeless forms a complex with Tipin to prevent the disassembly of the replisome (43). These findings suggest that mIDH1 inhibition induces genomic instability mediated by an increase in replication stress protein expression.

These findings were also confirmed in mIDH1 MGG119 GCCs that were untreated, treated with vehicle (DMSO), or 5μM AGI-5198 every 2 days for 1 week. Protein was extracted and the expression of PCNA and TIMELESS was determined using western blot analysis (Supplementary Figure 5). We observed a significant increase in PCNA protein expression in MGG119 cells treated with AGI-5198 compared to DMSO-treated cells ($p < 0.0001$)

(Supplementary Figure 5A-B). We observed a significant increase in TIMELESS protein expression in MGG119 treated with AGI-5198 compared to DMSO-treated cells ($p < 0.01$) (Supplementary Figure 5C-D).

We further validated our findings using both wt-IDH1 mouse NS and mIDH1 mouse NS. Protein was extracted and the expression of ZMYND8, TREX1, PCNA, and TIMELESS was determined using western blot analysis (Supplementary Figure 6). We observed a significant decrease in ZMYND8 protein expression in wt-IDH1 mouse NS ($p < 0.0001$) compared to mIDH1 mouse NS (Supplementary Figure 6A-B). We observed a significant increase in TREX1 protein expression in wt-IDH1 mouse NS ($p < 0.0001$) compared to mIDH1 mouse NS (Supplementary Figure 6C-D). Furthermore, we observed a significant increase in both PCNA ($p < 0.0001$) and TIMELESS ($p < 0.01$) protein expression in wt-IDH1 mouse NS compared to mIDH1 mouse NS (Supplementary Figure 6E-H).

Loss of ZMYND8 enhances the radiosensitivity of mIDH1 GCCs and exploits the vulnerability of mIDH1 GCCs to epigenetic inhibitors targeting BRD4 and HDAC

Based on the role of ZMYND8 in transcriptional repression at sites of DSB, we hypothesized that it might promote resistance to IR-induced DNA damage in mIDH1 GCCs. We began by targeting the human and mouse isoforms of ZMYND8 using short-hairpin (shRNA) knockdown that we cloned into our pT2-plasmid backbone (Supplementary Fig. S7A-B) (44,45). To confirm that the pT2-shZMYND8-GFP plasmids we designed could reduce ZMYND8 protein expression, we transfected HEK293 cells with pT2-shZMYND8-GFP plasmids targeting the human gene and NIH-3T3 cells for the mouse isoform in combination with the sleeping beauty transposase (SB) plasmid to improve the integration efficiency (9). We performed WB analysis 3 days post-transfection and observed a reduction in ZMYND8 expression in HEK293 transfected with human sh2-ZMYND8 and mouse sh4-ZMYND8 plasmids in NIH3T3 (Supplementary Fig. S7C).

Next, we generated stable ZMYND8 shRNA knockdown clones in two mIDH1 GCCs, SF10602 and MGG119. (Supplementary Fig. S8A). After purifying the GFP+ population by flow cytometry, we assessed ZMYND8 protein expression by WB in the MGG119 and SF10602 (Supplementary Fig. S8B and S8C). We observed a significant reduction of ZMYND8 protein expression by 75% in the MGG119 and 60% in the SF10602 compared to non-transfected (Supplementary Fig. S8D and S8E). Survival of mIDH1 GCCs expressing the shZMYND8-GFP plasmids was assessed 3 days post-irradiation exposure. MGG119 expressing the shZMYND8-GFP plasmids showed reduced cellular viability in response to escalating doses of radiation with a half maximal inhibitory concentration (IC_{50}) of 9.5Gy (Supplementary Fig. S8F). SF10602 expressing shZMYND8-GFP plasmids displayed a significant reduction in cellular viability but a IC_{50} was not reached at single radiation doses up to 20Gy (Supplementary Fig. S8G). These data suggest that suppression of ZMYND8 expression in mIDH1 GCC enhances their susceptibility to ionizing radiation.

Next, we ablated the expression of ZMYND8 using lentiviral CRISPRv2 vector expressing Cas9 and ZMYND8 guide RNAs (sgRNA) to generate ZMYND8 KO mIDH1 GCC clones (Fig. 4A) (20). After lentiviral incubation and puromycin selection, loss of ZMYND8 was evaluated by WB in the SF10602, MGG119 and NPAI mouse mIDH1 NS (Fig. 4B, 4C, and

4D respectively). We observed a significant reduction in cellular viability 3 days post-IR in the ZMYND8 KO compared to ZMYND8 WT mIDH1 GCCs. The SF10602 ZMYND8 KO had an IC_{50} of 7.5Gy compared to SF10602 ZMYND8 WT where an IC_{50} was not reached (Fig. 4E). The MGG119 ZMYND8 KO had an IC_{50} of 16.8Gy compared to MGG119 ZMYND8 WT where an IC_{50} was not reached (Fig. 4F). The NPAI ZMYND8 KO exhibited an IC_{50} of 2.8Gy versus the NPAI ZMYND8 WT where an IC_{50} was not reached. (Fig. 4G). These data indicate ZMYND8 contributes to the survival of mIDH1 GCCs in response to radiation.

Amplified expression of PDGFRA has been found in 9.9% of LGG, and was more frequently observed in diffuse astrocytoma (16.3%) as compared to oligodendroglioma (2.6%) (46). We developed a second mIDH1 mouse glioma model using the $PDGFRA^{D842V}$ plasmid to constitutively activate the receptor tyrosine kinase (RTK)-RAS-PI3K pathway (Supplementary Fig. S9A). We induced brain tumors in two experimental groups: wtIDH1 (RPA: $PDGFRA^{D842V}$, shP53, and shATRX) and mIDH1 (RPAI: $PDGFRA^{D842V}$, shP53, shATRX, and $mIDH1^{R132H}$). The MS of mice in the RPAI group was 172 days post-injection (DPI), which was significantly greater compared to RPA group with an MS of 92 DPI; $p<0.0023$, Mantel-Cox test (Supplementary Fig. S9B).

We generated the RPAI NS from a resected sleeping-beauty tumor 158 DPI, and integration of oncogenic plasmids was assessed by fluorescence microscopy (Supplementary Fig. S9C-D). Additionally, we demonstrated that the RPAI NS was able to generate tumors in mice and confirmed expression of mIDH1 using a specific antibody for the R132H mutation and ATRX loss by IHC (Supplementary Fig. S9E). WB analysis of RPAI NS treated with AGI-5198 revealed a decrease in global histone mark lysine trimethylation for H3K4me3, H3K27me3 and H3K36me3, but there was no change in global H3K27ac expression (Supplementary Fig. S9F). After we confirmed the loss of ZMYND8 in RPAI ZMYND8 KO by WB analysis (Supplementary Fig. S9G), we assessed their viability in response to IR. The RPAI ZMYND8 KO exhibited an IC_{50} of 4.0Gy versus the RPAI ZMYND8 WT with an IC_{50} of 8.1Gy (Supplementary Fig. S9H). This finding further supports the importance of ZMYND8 in survival of mIDH1-expression glioma cells to IR independent of the oncogenic driver mutation.

To begin to examine the mechanisms by which ZMYND8 contributes to genomic stability, we inhibited two newly described ZMYND8-interacting partners BRD4 and HDAC. We sought to investigate if BRD4 and HDAC cooperate with ZMYND8 to mediate the response to irradiation. We evaluated the sensitivity of our two mouse mIDH1 NS, NPAI ZMYND8 WT versus NPAI ZMYND8 KO and RPAI ZMYND8 WT versus RPAI ZMYND8 KO to two bromodomain and extraterminal domain inhibitors (BETi): JQ1 and I-BET-762, which also target BRD2 and BRD3 in addition to BRD4 (Fig. 4H). We also assessed the sensitivity of our mouse mIDH1 NS to the pan-histone deacetylase inhibitor Panobinostat, which targets Class I, II and IV HDACs (Fig. 4I). We observed an enhanced vulnerability of NPAI ZMYND8 KO to JQ1 treatment ($p < 0.0001$) with an IC_{50} of 0.18μM versus the NPAI ZMYND8 WT where an IC_{50} was not reached (Supplementary Fig. S10A). The RPAI ZMYND8 KO had a reduced viability to JQ1 ($p < 0.01$) with an IC_{50} of 0.51μM versus the RPAI ZMYND8 WT with an IC_{50} of 0.97μM (Supplementary Fig.

S10B). The NPAI ZMYND8 KO displayed reduced cellular viability to I-BET-762 ($p < 0.0001$) with an IC_{50} of 0.335μM versus the NPAI ZMYND8 WT where an IC_{50} was not reached (Supplementary Fig. S10C). The RPAI ZMYND8 KO displayed reduced viability to I-BET-762 ($p < 0.0001$) with an IC_{50} of 0.001μM versus the RPAI ZMYND8 WT with an IC_{50} of 0.19μM (Supplementary Fig. S10D). Both mouse NPAI NS displayed sensitivity to Panobinostat ($p < 0.0001$), with NPAI ZMYND8 WT having an IC_{50} of 0.0340μM versus NPAI ZMYND8 KO with an IC_{50} of 0.0075μM (Supplementary Fig. S10E). Similarly, both RPAI NS showed sensitivity to Panobinostat ($p < 0.0001$), with RPAI ZMYND8 KO having an IC_{50} of 0.0082μM versus RPAI ZMYND8 WT with an IC_{50} of 0.41μM (Supplementary Fig. S10F). We found that the NPAI ZMYND8 KO were more sensitive to BRD4 and HDAC inhibition compared to the NPAI ZMYND8 WT, which was also confirmed in the RPAI ZMYND8 KO versus RPAI ZMYND8 WT. The ZMYND8 KO mIDH1 GCCs exhibited higher levels of radiosensitization when IR was delivered in combination with either BRD4 or HDAC inhibition (Fig. 4J). Collectively, this data suggests the inhibition of epigenetic modulators BRD4 or HDAC in combination with IR further reduced the cellular viability of ZMYND8 KO mIDH1 GCCs.

Our results demonstrate that the changes in the sensitivity to BRD4 and HDAC inhibitors on ZMYND8-KO cells are directly related to the loss of ZMYND8 and not to changes on the expression of BRD4 and HDAC. Also, the expression of BRD4, HDAC1, and HDAC2 do not show a correlation with the expression levels of ZMYND8 (Supplementary Fig. S11).

These findings were further confirmed through mIDH1 MGG119 GCCs which were untreated, treated with vehicle (DMSO), or 5 μM AGI-5198 every 2 days for 1 week. Protein was extracted and the expression of HDAC1, HDAC2, and BRD4 was determined using western blot analysis (Supplementary Figure S12). We observed no significant difference in HDAC1 and HDAC2 protein expression between all three experimental groups (Supplementary Figure S12A-D). We observed a slight increase in the expression of BRD4 in MGG119 treated with AGI-5198 when compared with DMSO-treated cells ($p < 0.01$), however, this difference was not considered biologically meaningful (Supplementary Figure S12E-F).

In vivo impact of radiation on mIDH1 ZMYND8-WT and mIDH1 ZMYND8-KO models

Tumor-bearing mice were irradiated with a dose of 2Gy/day for 5 days each cycle (20 Gy total) for both experimental groups (Supplementary Fig. 13A-B). Tumor burden was confirmed using IVIS bioluminescence and radiation treatment started 10 days post tumor implantation. We observed a minor increase in the median survival mIDH1 (MS=18 days) vs. mIDH1+IR (MS=22 days) in the group with mIDH1 tumors (p=0.0045) (Supplementary Fig. 13C). The efficacy of radiation was more significant in mIDH1/ZMYND8 KO (MS=25 days) vs. mIDH1/ZMYND8KO+IR (MS=34 days) tumors (p=0.0084) (Supplementary Fig. S13D).

ZMYND8 KO mIDH1 GCCs are defective in resolving IR induced DNA damage and undergo activation of cell cycle arrest

To further examine the relationship between ZMYND8 and DDR signaling, we analyzed the activation of HR proteins at the indicated time points following 20Gy IR in SF10602 ZMYND8 WT and SF10602 ZMYND8 KO cells by WB (Fig. 5A). The HR pathway maintains genomic integrity by first sensing DNA damage, recruiting DNA repair mediators to the region and inducing cell cycle arrest (Fig. 5B). Gamma histone H2AX (γH2AX) has been used to assess DNA damage following IR but can also indicate genomic instability in the form of replication stress (47,48). We validated the loss of ZMYND8 expression in the SF10602 ZMYND8 KO (Fig. 5C) and quantified the changes in ZMYND8 expression within the SF10602 ZMYND8 WT post-IR (Fig. 5D). We observed sustained γH2AX signal in SF10602 ZMYND8 KO compared with SF10602 ZMYND8 WT following IR (Fig. 5C). SF10602 ZMYND8 KO display higher basal γH2AX signal in the non-irradiated (NR) control when compared with SF10602 ZMYND8 WT (Fig. 5E). The greatest difference in γH2AX expression relative to loading control (tubulin) was present at 24hrs post-IR ($p < 0.001$) (Fig. 5E). This delayed resolution of γH2AX signal may reflect a defect in the efficiency of DSB repair or an accumulation of DNA damage in the SF10602 ZMYND8 KO following IR. ATM is a master regulator of HR repair and undergoes autophosphorylation at serine 1981 (pATM), which actives ATM by dissociating it from a dimer to a monomer form (49). We observed enhanced activation of pATM in the SF10602 ZMYND8 KO compared to SF10602 ZMYND8 WT in response to IR (Fig. 5F). The greatest difference in pATM activation relative to β-actin was present at 30mins post-IR ($p < 0.001$) (Fig. 5G). DNA damage acquired during IR interrupts cell cycle progression through the activation of checkpoint kinases Chk1 and Chk2 to allow accurate DNA repair fidelity. As a safeguard, Chk1 triggers G2/M arrest in response to IR-induced DNA damage, its phosphorylation at serine 345 (pChk1) by ATR signifies impaired replication control (50). We observed extended activation of pChk1 relative to Chkl in SF10602 ZMYND8 KO compared to SF10602 ZMYND8 WT in response to IR (Fig. 5F). While the SF10602 ZMYND8 WT show a return of pChk1 to NR levels at 48hrs post-IR ($p < 0.0001$), the SF10602 ZMYND8 KO display prolonged activation of pChk1 (Fig. 5H).

Next, we evaluated phosphorylation of Rad51 at threonine 309 (pRad51), which is mediated by activated Chk1. Rad51 promotes genomic stability by binding to ssDNA to stabilize replication forks in order to protect under-replicated DNA regions during mitosis (51–53). Additionally, Rad51 is recruited to DSB regions where it cooperates with HR proteins to promote strand invasion (51). We observed elevated relative expression of pRad/Rad51 in SF10602 ZMYND8 KO compared to SF10602 ZMYND8 WT beginning at 4hrs post-IR ($p < 0.05$) which was most significantly elevated after 48hrs post IR ($p < 0.0001$) (Fig. 5I-J). Chk2 is phosphorylated on threonine 68 (pChk2) by ATM in order to induce G2/M arrest. We observed significant increase in the relative pChk2/Chk2 level in the SF10602 ZMYND8 KO compared to the SF10602 ZMYND8 WT beginning at 30mins post-IR ($p < 0.0001$) (Fig. 5K). While the SF10602 ZMYND8 WT show a return of pChk2 to NR levels at 24hrs post-IR ($p < 0.0001$), the SF10602 ZMYND8 KO display prolonged activation of pChk2 (Fig. 5K). These findings suggest that ZMYND8 plays an important role in DDR, which

is mediated by the mobilization of DDR proteins to repair IR-induced DNA damage and regulation of cell cycle progression.

ZMYND8 KO mIDH1 GCCs are more susceptible to PARP inhibition

Considering the elevated expression of DDR proteins following IR in ZMYND8 KO GCCs compared to ZMYND8 WT GCCs, we wondered if this resulted from an impaired resolution of DNA damage due to intrinsic genomic stress occurring within the ZMYND8 KO GCCs. We speculated that loss of ZMYND8 would increase the susceptibility of mIDH1 GCCs to chemicals that promote genotoxic stress. To evaluate this, we targeted PARP, an initial sensor of DNA lesions specifically at single-stranded DNA breaks (SSB) (Fig. 6A). PARP1 and PARP2 catalyze a reaction that utilizes NAD+ to attach negatively charged poly(ADP-ribose) polymers to various target proteins, including itself, to signal the recruitment of DNA repair proteins to the region. We choose to utilize Pamiparib, a selective PARP1/2 inhibitor which prevents PARP from binding to DNA, thus preventing the formation of PARP-DNA complexes which allow for the persistence of unrepaired SSB (Fig. 6A) (54). The PARP-DNA adducts create a barrier at replication forks, resulting in fork collapse and the formation of DSBs (Fig. 6A) (54). We observed a significant reduction ($p < 0.001$) in cellular viability of the SF10602 ZMYND8 KO to increasing doses of Pamiparib with an IC_{50} of 12.6μM versus the SF10602 ZMYND8 WT with an IC_{50} of 88.5 μM (Fig. 6B). When we combined Pamiparib with 20Gy IR, we observed enhanced therapeutic response in the SF10602 ZMYND8 KO compared to the SF10602 ZMYND8 WT (Fig. 6C). The sensitivity of SF10602 to Pamiparib +IR was further enhanced by the loss of ZMYND8, where this combination was also supported in the MGG119 (Supplementary Fig. S14A-B). Next, we evaluated the response of our mouse mIDH1 GCCs to PARP inhibition; we observed a significant reduction in cellular viability of NPAI ZMYND8 KO to Pamiparib alone with an IC_{50} of 4.9μM versus the NPAI ZMYND8 WT with an IC_{50} of 50.5μM (Fig. 6D). We also validated the response to Pamiparib in a second mIDH1 model (RPAI) *in vitro* presented in Supplementary Fig. S14C-D, which determines the efficacy of PARP inhibition and irradiation comparing mIDH1 ZMYND8 WT vs. mIDH1 ZMYND8 KO cells. Comparably, RPAI ZMYND8 KO glioma cells displayed a significant reduction in cellular viability when treated with Pamiparib (IC_{50} = 2.0μM; $p < 0.0001$) vs. RPAI ZMYND8 WT glioma cells (IC_{50} = 44.7μM) (Supplementary Fig. S14C). In the combination of Pamiparib and 6Gy IR, we similarly observed an enhanced therapeutic response in the NPAI ZMYND8 KO compared to the NPAI ZMYND8 WT (Fig. 6E). Additionally, the combination of Pamiparib with IR (6 Gy) significantly ($p < 0.01$) reduced cellular viability of RPAI ZMYND8 KO glioma cells compared to RPAI ZMYND8 WT glioma cells at all concentration of Pamiparib used (Supplementary Fig. S14D). The recruitment of ZMYND8 to regions of DNA damage has been proposed to be mediated by PARP (15). These data suggest that PARP could function upstream of ZMYND8. To translate these findings to *in vivo*, we implanted 50,000 NPAI ZMYND8 WT GCCs in immunocompetent C57BL6 mice and confirmed tumor burden based on IVIS bioluminescence signal at 10 days post implantation (dpi). Tumor bearing mice were administered saline or Pamiparib (1mg/mL) and with/out IR, as indicated in Figure 6F. We observed a 1.7-fold ($p < 0.05$) increase in the MS of mice in the Pamiparib + IR group (MS: 55dpi) when compared to IR alone (MS: 38 dpi) or Pamiparib alone (MS:34 dpi) (Fig. 6G). When compared to the control mice

that received saline (MS:29 dpi), mice in the Pamiparib + IR group displayed a 1.9-fold ($p<0.01$) increase in MS (Fig. 6G). We did not observe a significant difference in viability in response to AGI-5198 treatment in NPAI ZMYND8 WT versus ZMYND8 KO, but when combined with IR we observed a modest reduction in viability $p<0.05$ (Fig. 6H). The enhanced sensitivity of mIDH1 GCCs to IR after the genetic knockout of ZMYND8, or treatment with HDAC or PARP inhibitors, propose a novel vulnerability of mIDH1 GCCs to respond to IR-induced DNA damage. We speculate that the loss of transcriptional repression mediated by ZMYND8's recruitment of NuRD or ZMYND8 recognition of DNA damaged regions marked by PARP leads to defective HR repair in mIDH1 GCCs (Fig. 6I).

To address whether ZMYND8 expression varied across LGG patients based on IDH1 mutation status, we analyzed publicly available RNA-seq data from the The Cancer Genome Atlas (TCGA) LGG dataset (Supplementary Fig. S15A). We observed a significant increase ($p<0.05$) in log2-normalized ZMYND8 expression in mIDH1 LGG versus wtIDH1 LGG. When we stratified the overall survival (OS) of LGG patient into low- or high-ZMYND8 expression groups, we found that high-ZMYND8 mIDH1 LGG were associated with poor clinical outcome with a median OS of 6.3yrs as compared with low-ZMYND8 mIDH1 LGG with a median OS of 7.9yrs (Supplementary Fig. S15B). There was no significant difference found within wtIDH1 LGGs, where high-ZMYND8 wtIDH1 LGGs had a median OS of 1.7yrs compared with 2.0yrs in low-ZMYND8 wtIDH1 LGGs. This significant discrepancy in OS found amongst mIDH1 LGGs ($p<0.0001$), indicates that a subset of mIDH1 glioma overexpress ZMYND8 and of which present with poor patient outcome. Considering that upon recurrence IDH-mutated gliomas present as high-grade, we analyzed Kaplan Meier survival for median ZMYND8 expression along with mIDH1 status from the Chinese Glioma Genome Atlas (CGGA) for primary and secondary GBM (Supplementary Fig. S15C-F). There was no significant discrepancy in median OS found amongst CGGA primary (Supplementary Fig. S15C) or secondary (Supplementary Fig. S15D) wtIDH1 GBM based on ZMYND8 median expression. We observed a shortening in median OS within primary (Supplementary Fig. S15E, $p < 0.0014$) and secondary (Supplementary Fig. S15F, $p < 0.0027$) mIDH1 GBM high-ZMYND8 compared to low-ZMYND8 patient tumors.

We performed serum biochemistry analysis of liver and kidney metabolites in the animals receiving Pamiparib, or Pamiparib + IR treatment compared with animals in the saline treatment group. There was no significant difference observed in the serum level of kidney (creatinine, blood urea nitrogen) and liver (aminotransferase, aspartate aminotransferase) metabolites tested in animals treated with Pamiparib, or Pamiparib + IR treatment compared to saline treatment group (Supplementary Fig. 16).

Histopathological analysis of liver sections to inspect the potential toxicity of the Pamiparib+IR treatment revealed that the liver tissue sections had no differences in the hepatocytes, stromal central, and portal areas between the control saline and the treatment group (Supplemental Fig. 17).

Discussion

IDH-mutant gliomas represent a distinct molecular subtype of brain cancer defined by the presence of DNA hypermethylation commonly referred to as CpG island methylator phenotype (CIMP) and dysregulation in the removal of histone lysine trimethylation (7,8). This epigenetic reprogramming mechanism is dependent upon the production of 2HG by mIDH1, which notably our group and others have demonstrated can be reversed through treatment with mIDH1 specific inhibitors (9,10,31,55). A shared feature across IDH1/2 mutant cancers showed a high propensity of DNA hypermethylated regions at gene bodies and enhancers, while surprisingly the majority of gene promoters remained hypomethylated (55). Although this finding might imply a universal effect of the IDH-mutation, another study revealed distinct methylome patterns when comparing IDH-mutant tumors to IDH-wildtype tissue matched counterparts. The authors found that 19% of CpG sites were exclusively hypermethylated in IDH-mutant glioma compared to 3% in IDH-mutant AML, 2% in melanoma, and 4% in cholangiocarcinoma (56). CpG methylation can impact nearby genes altering their expression, thus these differentially methylated regions across IDH-mutant cancers may be dependent upon the cellular origin of the cancer. IDH-mutant gliomas displayed the greatest number of biological pathway alterations compared with the other tumor types, specifically the downregulation of tissue development and an upregulation of a subset of DNA repair pathways (56).

To date, our understanding of the reversibility of histone hypermethylation following loss of mIDH1 activity has been limited to immortalized human astrocytes (IHA) that expressed mIDH1 under a doxycycline (dox) inducible system (7). Notably, IHA-expressing mIDH1 displayed upregulation of stem-like genes: *CD24* and *PDGFRA*, which was accompanied by a transient gain of H3K4me3 at these gene promoter regions suggesting that mIDH1 poises these genes for activation. Following dox-withdrawal, methylation at most loci eventually returned to baseline levels either transiently (13.8%) or gradually (62.5%) across cell passages, but 23.7% of regions persisted after loss of mIDH1. These findings suggest that the epigenetic reprogramming mediated by mIDH1 is still not well understood, especially in regard to the contribution of mIDH1 regulation on genes involved in therapeutic resistance to radiation treatment.

Given that mIDH1-R132H is endogenously expressed in SF10602 and was derived from a patient tumor subjected to radiotherapy, we sought to determine mIDH1-dependent mechanisms that contributed to radioresistance (27). We found that ZMYND8 was significantly downregulated following mIDH1 inhibition in the SF10602 treated with AGI-5198. Recent studies have reported that ZMYND8's recruitment to regions of laser-microirradation induced DNA damage is important to facilitate HR DNA repair (12,14,15). In doing so, ZMYND8 functions as a beacon to direct the NuRD complex to damaged DNA regions and allow for repression of transcription (12,15). The acetylated histone residues H3K14ac and H4K16ac, which are recognized by ZMYND8, have been shown to be crucial for DNA checkpoint activation and local HR repair of DSB (57,58). Recent studies have demonstrated preferential vulnerability of mIDH1-expressing glioma models to inhibitors targeting HDAC, which is a component of the NuRD complex (59,60). Interestingly, mIDH1

glioma cells treated with Panobinostat displayed increased H3K14ac, which is recognized by ZMYND8 (60).

Our current findings provide evidence that ZMYND8 is epigenetically regulated in human mIDH1 GCCs based on the loss of active histone mark H3K4me3 at the ZMYND8 promoter locus following mIDH1 inhibition. Additionally, our comparison of mouse mIDH1 NS vs. wtIDH1 NS demonstrated that mouse mIDH1 NS had an enhanced enrichment of H3K4me3 at the ZMYND8 promoter locus by ChIP-seq and increased nascent transcription by Bru-seq. To our knowledge, a direct connection between ZMYND8 regulation at the chromatin level within mIDH1 glioma has not previously been described. However, we found that high ZMYND8 expressing mIDH1 LGG patient tumors exhibited a shorter median OS as compared with low ZMYND8 expressing mIDH1 LGG. In the context of brain cancer, ZMYND8 has been shown to preferentially bind histone 3.3 point mutant G34R (H3.3G34R) present in pediatric high grade glioma to suppress genes involved in MHC II presentation (21).

We observed a significant reduction in ZMYND8 protein expression in three patient-derived mIDH1 GCC after treatment with DS-1001b. Additionally, inhibition of mIDH1 in SF10602 increased expression of genes associated with replication stress and genomic instability. Timeless has been shown to accumulate at regions of DNA damage tracks induced by laser-microirradiation and its retention at damaged chromatin is dependent on the presence of PARP but not its activity (61,62). Cancer cells undergo persistent DNA replication stress as a result of aberrant cell cycle progression. Timeless has been shown to stabilize replication forks and contribute to sister chromatid cohesion for maintenance of genomic integrity (63,64). In cervical cancer models, the overexpression of Timeless has been proposed to function in response to replication stress driven by oncogene activation (65). TREX1 is known to function as a 3’-5’ DNA exonuclease to degrade ssDNA or mispaired DNA duplexes that arise from the repair of DNA lesions and aberrant replication (38,52). The elevated expression of Timeless and TREX1 following mIDH1 inhibition in SF10602 could be an indication of enhanced genomic stress.

By selectively suppressing ZMYND8 expression in human mIDH1 GCCs by the means of shRNA knockdown or genetic knockout using lenti-CRISPRCas9, we observed a significant decrease in cellular viability in response to IR. Additionally, inhibition of epigenetic regulators BRD4 and HDAC further reduced the viability of ZMYND8 KO mIDH1 GCCs. Recent work in AML showed that ZMYND8 recruitment to enhancers was mediated by BRD4 (22). The oncogenic programs regulated by BRD4 to support cancer cell survival were downregulated in AMLs when ZMYND8 was depleted (22). Inhibition of BRD4 using JQ1 was shown to abolish ZMYND8 occupancy at enhancers (22). There is compelling evidence that BRD4 functions at replication forks, where it associates with several complexes involved in chromatin remodeling (MMS22L, TONSL) and replication (POLA2, POLD3), which we also observed to be upregulated in our RNA-seq analysis (66). Additionally, inhibition of BRD4 either by siRNA knockdown or JQ1 treatment has been shown to induce DNA damage marked by increased γH2AX foci formation (67). Loss of BRD4 induces replicative stress via the deregulation of transcription and in response RAD51 is recruited to damaged DNA regions to suppress replication (68).

Traditionally, BRD4 inhibitors like JQ1 compete with the acetyl lysine recognition binding site on BRD4 preventing its ability to facilitate oncogenic transcription at enhancers leading to a suppression of cancer cell growth and apoptosis (69). More recently, degradation of BRD4 has been shown to induce endogenous DNA damage in cancer cells undergoing replication marked by an increase in γH2AX foci (70). It is likely that the differences in cellular viability of mouse mIDH1 ZMYND8 KO and ZMYND8 WT treated with JQ1/I-BET-762 could be the result of enhanced DNA damage facilitated by inhibition of BRD4 in ZMYND8 KO cells. Treatment of mIDH1 tumor cells with the HDAC inhibitor Vorinostat lead to a suppression of Rad51 and Brca1 expression, along with an increase in cleaved PARP (59). HDAC inhibitors have been shown to increase histone acetylation (H3K9, H3K18, H3K56, H4K8, H4K16) and induce senescence mediated by p21 and p27 (71). It has been proposed that the hyperacetylation of histone prevents chromatin condensation, a necessary step for DNA repair. While also downregulating the expression of key DNA repair proteins like Ku70, DNA-Pkc, and Rad51 (72). HDAC inhibitors exhibit broad antineoplastic effects mediated by the induction of apoptosis, cell cycle arrest and inhibition of DNA repair machinery. Our data suggest that the susceptibility of mIDH1 glioma cells to either BRD4 or HDAC inhibitors is dependent on the expression of ZMYND8. Our data also suggests that BRD4 or HDAC expression levels are not correlated with the levels of ZMYND8 expression.

In support of the role of ZMYND8 in genomic integrity, loss of ZMYND8 in triple-negative breast cancer cells lead to an increase in micronuclei formation along with chromosome aberrations including dicentric chromosomes and DNA breaks evaluated by metaphase spreads (20). A potential mechanism contributing to this induction of genomic instability, could be the result of overactivation of enhancers following the loss of ZMYND8 (57). A recent study mapping transcription-mediated DSB in breast cancer revealed that RAD51 localized to super-enhancers to stabilize DNA damage occurring due to hypertranscription (73).

In our time-course assessment of HR repair protein activation following IR, SF10602 ZMYND8 KO displayed prolonged activation of pChk2, while the SF10602 ZMYND8 WT showed a return to baseline 24hrs post-IR. It has been proposed that ZMYND8 functions in transcriptional silencing of active transcription leading to an increase in DNA damage (12). Over time, the impaired DNA repair leads to sustained expression of DDR proteins (12). We hypothesize that loss of ZMYND8 impairs the resolution of DSB induced by IR, which leads to extended cell cycle arrest mediated by pChk2.

PARP functions as an early sensor of DNA damage and has been shown to rapidly deposit poly-ADP ribose chains (PARylation) at newly generated DNA DSB within milliseconds (74). The recruitment of ZMYND8 to laser-induced DSB was shown to be dependent upon the presence of PARylation (15). Surprisingly, we observed that ZMYND8 WT mIDH1 glioma cells were sensitive to Pamiparib treatment, but ZMYND8 KO mIDH1 glioma cells displayed a further decrease in cellular viability. Recent studies have observed enhanced sensitivity of IDH-mutant glioma to PARP inhibition using preclinical mouse models and human glioma stem cell lines (75,76). Pamiparib (BGB-290) in combination with TMZ is currently being evaluated clinically for the treatment of IDH1/2 mutant grade I-IV Gliomas

(NCT03749187) and recurrent gliomas with IDH1/2 mutations (NCT03914742). Moreover, our data shows that ZMYND8 functions alongside PARP to signal the repair of IR induced DNA damage.

PARP inhibitors and antibodies that inhibit immune checkpoints, like CTLA-4, PD-1 and PD-L1 are currently being evaluated in clinical trials for ovarian, breast, prostate, lung, urothelial, and gastrointestinal cancers (77). In preclinical models of breast cancer, PARP inhibitors have been shown to upregulate the expression of PD-L1 (78). To date, clinical trials in recurrent IDH-mutant glioma are recruiting patients to evaluate PARP inhibitors alone and in combination with chemotherapeutic agents like temozolomide and carboplatin (79). Also, the combination of Olaparib, a PARP inhibitor, and durvalumab, a PD-L1 antibody, is currently being investigated in patients with recurrent IDH-mutated high-grade glioma (80).

In summary, by examining the alterations to the epigenome and biological pathways following mIDH1 inhibition, we provide novel evidence that ZMYND8 is epigenetically regulated by mIDH1 reprogramming in patient derived mIDH1 GCCs and in our genetically engineered mouse mIDH1 glioma model. In addition, our data shows that ZMYND8 supports the survival of human mIDH1 GCCs and mouse mIDH1 NS in response to radiation through its role in contributing to DNA repair and genomic stability. Genetic ablation of ZMYND8 in combination with epigenetic inhibitors against PARP, HDAC, and BRD4 further reduces the cellular viability of mIDH1 GCCs to IR induced DNA damage. We anticipate these findings will provide support for the development of ZMYND8 specific inhibitors, which represents a viable target for the treatment of mIDH1 gliomas.

Supplementary Material

Refer to Web version on PubMed Central for supplementary material.

Acknowledgments

We thank Dr. D. Cahill (Harvard Medical School) and Dr. H. Wakimoto for providing the mIDH1 human glioma cells MGG119 and Dr. J. Costello (UCSF) for providing the mIDH1 human glioma cells SF10602, which were a gift from the Dabbiere Family and funded by NIH/NCI R01CA244838; Dr. M. Luo and Dr. W. Luo for providing the lentiviral ZMYND8 CRISPRv2 plasmid; and Dr. J. Ohlfest (University of Minnesota, deceased) for providing the SB model plasmids.

Financial Support:

This work was supported by the National Institutes of Health/National Institute of Neurological Disorders & Stroke (NIH/NINDS) Grants R37-NS094804, R01-NS105556, R01-NS122536, R01-NS124167, R21-NS123879-01 and Rogel Cancer Center Scholar Award to M.G.C.; NIH/NINDS Grants R01-NS076991, R01-NS082311, R01-NS096756, R01NS122234; and NIH/NCI R01-CA243916 to P.R.L.; the Department of Neurosurgery; the Pediatric Brain Tumor Foundation, Leah's Happy Hearts Foundation, Ian's Friends Foundation (IFF), Chad Tough Foundation, and Smiles for Sophie Forever Foundation to [M.G.C. and P.R.L]. S. Carney was supported by the University of Michigan Rackham Merit Fellowship, NIH/NCI-T32-CA009676 Grant and PA18-906 NIH/NINDS Diversity Minority Supplement.

References

1. Bai H, Harmancı AS, Erson-Omay EZ, Li J, Coşkun S, Simon M, et al. Integrated genomic characterization of IDH1-mutant glioma malignant progression. Nat Genet 2016;48(1):59–66 doi 10.1038/ng.3457. [PubMed: 26618343]
2. Ceccarelli M, Barthel FP, Malta TM, Sabedot TS, Salama SR, Murray BA, et al. Molecular Profiling Reveals Biologically Discrete Subsets and Pathways of Progression in Diffuse Glioma. Cell 2016;164(3):550–63 doi 10.1016/j.cell.2015.12.028. [PubMed: 26824661]
3. Arita H, Kinoshita M, Kawaguchi A, Takahashi M, Narita Y, Terakawa Y, et al. Lesion location implemented magnetic resonance imaging radiomics for predicting IDH and TERT promoter mutations in grade II/III gliomas. Sci Rep 2018;8(1):11773 doi 10.1038/s41598-018-30273-4. [PubMed: 30082856]
4. Yan H, Parsons DW, Jin G, McLendon R, Rasheed BA, Yuan W, et al. IDH1 and IDH2 mutations in gliomas. N Engl J Med 2009;360(8):765–73 doi 10.1056/NEJMoa0808710. [PubMed: 19228619]
5. Miller JJ, Loebel F, Juratli TA, Tummala SS, Williams EA, Batchelor TT, et al. Accelerated progression of IDH mutant glioma after first recurrence. Neuro Oncol 2019;21(5):669–77 doi 10.1093/neuonc/noz016. [PubMed: 30668823]
6. Halasz LM, Attia A, Bradfield L, Brat DJ, Kirkpatrick JP, Laack NN, et al. Radiation Therapy for IDH-Mutant Grade 2 and Grade 3 Diffuse Glioma: An ASTRO Clinical Practice Guideline. Practical Radiation Oncology 2022 doi 10.1016/j.prro.2022.05.004.
7. Turcan S, Makarov V, Taranda J, Wang Y, Fabius AWM, Wu W, et al. Mutant-IDH1-dependent chromatin state reprogramming, reversibility, and persistence. Nat Genet 2018;50(1):62–72 doi 10.1038/s41588-017-0001-z. [PubMed: 29180699]
8. Turcan S, Rohle D, Goenka A, Walsh LA, Fang F, Yilmaz E, et al. IDH1 mutation is sufficient to establish the glioma hypermethylator phenotype. Nature 2012;483(7390):479–83 doi 10.1038/nature10866. [PubMed: 22343889]
9. Nunez FJ, Mendez FM, Kadiyala P, Alghamri MS, Savelieff MG, Garcia-Fabiani MB, et al. IDH1-R132H acts as a tumor suppressor in glioma via epigenetic up-regulation of the DNA damage response. Sci Transl Med 2019;11(479) doi 10.1126/scitranslmed.aaq1427.
10. Kadiyala P, Carney SV, Gauss JC, Garcia-Fabiani MB, Haase S, Alghamri MS, et al. Inhibition of 2-hydroxyglutarate elicits metabolic reprogramming and mutant IDH1 glioma immunity in mice. J Clin Invest 2021;131(4) doi 10.1172/JCI139542.
11. Rohle D, Popovici-Muller J, Palaskas N, Turcan S, Grommes C, Campos C, et al. An inhibitor of mutant IDH1 delays growth and promotes differentiation of glioma cells. Science 2013;340(6132):626–30 doi 10.1126/science.1236062. [PubMed: 23558169]
12. Gong F, Chiu LY, Cox B, Aymard F, Clouaire T, Leung JW, et al. Screen identifies bromodomain protein ZMYND8 in chromatin recognition of transcription-associated DNA damage that promotes homologous recombination. Genes Dev 2015;29(2):197–211 doi 10.1101/gad.252189.114. [PubMed: 25593309]
13. Savitsky P, Krojer T, Fujisawa T, Lambert JP, Picaud S, Wang CY, et al. Multivalent Histone and DNA Engagement by a PHD/BRD/PWWP Triple Reader Cassette Recruits ZMYND8 to K14ac-Rich Chromatin. Cell Rep 2016;17(10):2724–37 doi 10.1016/j.celrep.2016.11.014. [PubMed: 27926874]
14. Gong F, Clouaire T, Aguirrebengoa M, Legube G, Miller KM. Histone demethylase KDM5A regulates the ZMYND8-NuRD chromatin remodeler to promote DNA repair. J Cell Biol 2017;216(7):1959–74 doi 10.1083/jcb.201611135. [PubMed: 28572115]
15. Spruijt CG, Luijsterburg MS, Menafra R, Lindeboom RG, Jansen PW, Edupuganti RR, et al. ZMYND8 Co-localizes with NuRD on Target Genes and Regulates Poly(ADP-Ribose)-Dependent Recruitment of GATAD2A/NuRD to Sites of DNA Damage. Cell Rep 2016;17(3):783–98 doi 10.1016/j.celrep.2016.09.037. [PubMed: 27732854]
16. Ghosh K, Tang M, Kumari N, Nandy A, Basu S, Mall DP, et al. Positive Regulation of Transcription by Human ZMYND8 through Its Association with P-TEFb Complex. Cell Rep 2018;24(8):2141–54 e6 doi 10.1016/j.celrep.2018.07.064. [PubMed: 30134174]

17. Chen Y, Zhang B, Bao L, Jin L, Yang M, Peng Y, et al. ZMYND8 acetylation mediates HIF-dependent breast cancer progression and metastasis. J Clin Invest 2018;128(5):1937–55 doi 10.1172/JCI95089. [PubMed: 29629903]
18. Pan Q, Zhong S, Wang H, Wang X, Li N, Li Y, et al. The ZMYND8-regulated mevalonate pathway endows YAP-high intestinal cancer with metabolic vulnerability. Mol Cell 2021;81(13):2736–51 e8 doi 10.1016/j.molcel.2021.04.009. [PubMed: 33932349]
19. Li N, Li Y, Lv J, Zheng X, Wen H, Shen H, et al. ZMYND8 Reads the Dual Histone Mark H3K4me1-H3K14ac to Antagonize the Expression of Metastasis-Linked Genes. Mol Cell 2016;63(3):470–84 doi 10.1016/j.molcel.2016.06.035. [PubMed: 27477906]
20. Wang Y, Luo M, Chen Y, Wang Y, Zhang B, Ren Z, et al. ZMYND8 Expression in Breast Cancer Cells Blocks T-Lymphocyte Surveillance to Promote Tumor Growth. Cancer Res 2021;81(1):174–86 doi 10.1158/0008-5472.CAN-20-1710. [PubMed: 33148660]
21. Jiao F, Li Z, He C, Xu W, Yang G, Liu T, et al. RACK7 recognizes H3.3G34R mutation to suppress expression of MHC class II complex components and their delivery pathway in pediatric glioblastoma. Sci Adv 2020;6(29):eaba2113 doi 10.1126/sciadv.aba2113. [PubMed: 32832624]
22. Cao Z, Budinich KA, Huang H, Ren D, Lu B, Zhang Z, et al. ZMYND8-regulated IRF8 transcription axis is an acute myeloid leukemia dependency. Mol Cell 2021;81(17):3604–22 e10 doi 10.1016/j.molcel.2021.07.018. [PubMed: 34358447]
23. Tang B, Sun R, Wang D, Sheng H, Wei T, Wang L, et al. ZMYND8 preferentially binds phosphorylated EZH2 to promote a PRC2-dependent to -independent function switch in hypoxia-inducible factor-activated cancer. Proc Natl Acad Sci U S A 2021;118(8) doi 10.1073/pnas.2019052118.
24. Serresi M, Kertalli S, Li L, Schmitt MJ, Dramaretska Y, Wierikx J, et al. Functional antagonism of chromatin modulators regulates epithelial-mesenchymal transition. Sci Adv 2021;7(9) doi 10.1126/sciadv.abd7974.
25. Shiota H, Elya JE, Alekseyenko AA, Chou PM, Gorman SA, Barbash O, et al. "Z4" Complex Member Fusions in NUT Carcinoma: Implications for a Novel Oncogenic Mechanism. Mol Cancer Res 2018;16(12):1826–33 doi 10.1158/1541-7786.MCR-18-0474. [PubMed: 30139738]
26. Choi S, Lee KW, Koh HH, Park S, Yeo SY, Joh JW, et al. Validation of ZMYND8 as a new treatment target in hepatocellular carcinoma. J Cancer Res Clin Oncol 2021;147(12):3517–34 doi 10.1007/s00432-021-03768-3. [PubMed: 34462784]
27. Jones LE, Hilz S, Grimmer MR, Mazor T, Najac C, Mukherjee J, et al. Patient-derived cells from recurrent tumors that model the evolution of IDH-mutant glioma. Neurooncol Adv 2020;2(1):vdaa088 doi 10.1093/noajnl/vdaa088. [PubMed: 32904945]
28. Wakimoto H, Tanaka S, Curry WT, Loebel F, Zhao D, Tateishi K, et al. Targetable signaling pathway mutations are associated with malignant phenotype in IDH-mutant gliomas. Clin Cancer Res 2014;20(11):2898–909 doi 10.1158/1078-0432.CCR-13-3052. [PubMed: 24714777]
29. Mendez FM, Nunez FJ, Zorrilla-Veloz RI, Lowenstein PR, Castro MG. Native Chromatin Immunoprecipitation Using Murine Brain Tumor Neurospheres. J Vis Exp 2018(131) doi 10.3791/57016.
30. Núñez Felipe J, Mendez Flor M, Kadiyala P, Alghamri Mahmoud S, Savelieff Masha G, Garcia-Fabiani Maria B, et al. IDH1-R132H acts as a tumor suppressor in glioma via epigenetic up-regulation of the DNA damage response. Science Translational Medicine 2019;11(479):eaaq1427 doi 10.1126/scitranslmed.aaq1427. [PubMed: 30760578]
31. Tateishi K, Wakimoto H, Iafrate AJ, Tanaka S, Loebel F, Lelic N, et al. Extreme Vulnerability of IDH1 Mutant Cancers to NAD+ Depletion. Cancer Cell 2015;28(6):773–84 doi 10.1016/j.ccell.2015.11.006. [PubMed: 26678339]
32. Petropoulos M, Champeris Tsaniras S, Taraviras S, Lygerou Z. Replication Licensing Aberrations, Replication Stress, and Genomic Instability. Trends Biochem Sci 2019;44(9):752–64 doi 10.1016/j.tibs.2019.03.011. [PubMed: 31054805]
33. Gaillard H, Garcia-Muse T, Aguilera A. Replication stress and cancer. Nat Rev Cancer 2015;15(5):276–89 doi 10.1038/nrc3916. [PubMed: 25907220]

34. Saredi G, Huang H, Hammond CM, Alabert C, Bekker-Jensen S, Forne I, et al. H4K20me0 marks post-replicative chromatin and recruits the TONSL-MMS22L DNA repair complex. Nature 2016;534(7609):714–8 doi 10.1038/nature18312. [PubMed: 27338793]
35. Tsutakawa SE, Classen S, Chapados BR, Arvai AS, Finger LD, Guenther G, et al. Human flap endonuclease structures, DNA double-base flipping, and a unified understanding of the FEN1 superfamily. Cell 2011;145(2):198–211 doi 10.1016/j.cell.2011.03.004. [PubMed: 21496641]
36. Cali F, Bharti SK, Di Perna R, Brosh RM, Jr., Pisani FM. Tim/Timeless, a member of the replication fork protection complex, operates with the Warsaw breakage syndrome DNA helicase DDX11 in the same fork recovery pathway. Nucleic Acids Res 2016;44(2):705–17 doi 10.1093/nar/gkv1112. [PubMed: 26503245]
37. Hambarde S, Tsai CL, Pandita RK, Bacolla A, Maitra A, Charaka V, et al. EXO5-DNA structure and BLM interactions direct DNA resection critical for ATR-dependent replication restart. Mol Cell 2021;81(14):2989–3006 e9 doi 10.1016/j.molcel.2021.05.027. [PubMed: 34197737]
38. Mohr L, Toufektchan E, von Morgen P, Chu K, Kapoor A, Maciejowski J. ER-directed TREX1 limits cGAS activation at micronuclei. Mol Cell 2021;81(4):724–38 e9 doi 10.1016/j.molcel.2020.12.037. [PubMed: 33476576]
39. Gong Z, Kim JE, Leung CC, Glover JN, Chen J. BACH1/FANCJ acts with TopBP1 and participates early in DNA replication checkpoint control. Mol Cell 2010;37(3):438–46 doi 10.1016/j.molcel.2010.01.002. [PubMed: 20159562]
40. Xie L, Pi X, Mishra A, Fong G, Peng J, Patterson C. PHD3-dependent hydroxylation of HCLK2 promotes the DNA damage response. J Clin Invest 2012;122(8):2827–36 doi 10.1172/JCI62374. [PubMed: 22797300]
41. Cancino GI, Fatt MP, Miller FD, Kaplan DR. Conditional ablation of p63 indicates that it is essential for embryonic development of the central nervous system. Cell Cycle 2015;14(20):3270–81 doi 10.1080/15384101.2015.1087618. [PubMed: 26359534]
42. Yang YG, Lindahl T, Barnes DE. Trex1 exonuclease degrades ssDNA to prevent chronic checkpoint activation and autoimmune disease. Cell 2007;131(5):873–86 doi 10.1016/j.cell.2007.10.017. [PubMed: 18045533]
43. Yoshizawa-Sugata N, Masai H. Human Tim/Timeless-interacting protein, Tipin, is required for efficient progression of S phase and DNA replication checkpoint. J Biol Chem 2007;282(4):2729–40 doi 10.1074/jbc.M605596200. [PubMed: 17102137]
44. Calinescu AA, Nunez FJ, Koschmann C, Kolb BL, Lowenstein PR, Castro MG. Transposon mediated integration of plasmid DNA into the subventricular zone of neonatal mice to generate novel models of glioblastoma. J Vis Exp 2015(96) doi 10.3791/52443.
45. Koschmann C, Calinescu AA, Nunez FJ, Mackay A, Fazal-Salom J, Thomas D, et al. ATRX loss promotes tumor growth and impairs nonhomologous end joining DNA repair in glioma. Sci Transl Med 2016;8(328):328ra28 doi 10.1126/scitranslmed.aac8228.
46. Motomura K, Mittelbronn M, Paulus W, Brokinkel B, Keyvani K, Sure U, et al. PDGFRA gain in low-grade diffuse gliomas. J Neuropathol Exp Neurol 2013;72(1):61–6 doi 10.1097/NEN.0b013e31827c4b5b. [PubMed: 23242283]
47. Banath JP, Klokov D, MacPhail SH, Banuelos CA, Olive PL. Residual gammaH2AX foci as an indication of lethal DNA lesions. BMC Cancer 2010;10:4 doi 10.1186/1471-2407-10-4. [PubMed: 20051134]
48. Mah LJ, El-Osta A, Karagiannis TC. gammaH2AX: a sensitive molecular marker of DNA damage and repair. Leukemia 2010;24(4):679–86 doi 10.1038/leu.2010.6. [PubMed: 20130602]
49. So S, Davis AJ, Chen DJ. Autophosphorylation at serine 1981 stabilizes ATM at DNA damage sites. J Cell Biol 2009;187(7):977–90 doi 10.1083/jcb.200906064. [PubMed: 20026654]
50. Wilsker D, Petermann E, Helleday T, Bunz F. Essential function of Chk1 can be uncoupled from DNA damage checkpoint and replication control. Proc Natl Acad Sci U S A 2008;105(52):20752–7 doi 10.1073/pnas.0806917106. [PubMed: 19091954]
51. Wassing IE, Graham E, Saayman X, Rampazzo L, Ralf C, Bassett A, et al. The RAD51 recombinase protects mitotic chromatin in human cells. Nat Commun 2021;12(1):5380 doi 10.1038/s41467-021-25643-y. [PubMed: 34508092]

52. Wolf C, Rapp A, Berndt N, Staroske W, Schuster M, Dobrick-Mattheuer M, et al. RPA and Rad51 constitute a cell intrinsic mechanism to protect the cytosol from self DNA. Nat Commun 2016;7:11752 doi 10.1038/ncomms11752. [PubMed: 27230542]
53. Adolph MB, Mohamed TM, Balakrishnan S, Xue C, Morati F, Modesti M, et al. RADX controls RAD51 filament dynamics to regulate replication fork stability. Mol Cell 2021;81(5):1074–83 e5 doi 10.1016/j.molcel.2020.12.036. [PubMed: 33453169]
54. Li H, Liu ZY, Wu N, Chen YC, Cheng Q, Wang J. PARP inhibitor resistance: the underlying mechanisms and clinical implications. Mol Cancer 2020;19(1):107 doi 10.1186/s12943-020-01227-0. [PubMed: 32563252]
55. Urban DJ, Martinez NJ, Davis MI, Brimacombe KR, Cheff DM, Lee TD, et al. Assessing inhibitors of mutant isocitrate dehydrogenase using a suite of pre-clinical discovery assays. Sci Rep 2017;7(1):12758 doi 10.1038/s41598-017-12630-x. [PubMed: 28986582]
56. Bledea R, Vasudevaraja V, Patel S, Stafford J, Serrano J, Esposito G, et al. Functional and topographic effects on DNA methylation in IDH1/2 mutant cancers. Sci Rep 2019;9(1):16830 doi 10.1038/s41598-019-53262-7. [PubMed: 31727977]
57. Shen H, Xu W, Guo R, Rong B, Gu L, Wang Z, et al. Suppression of Enhancer Overactivation by a RACK7-Histone Demethylase Complex. Cell 2016;165(2):331–42 doi 10.1016/j.cell.2016.02.064. [PubMed: 27058665]
58. Horikoshi N, Sharma D, Leonard F, Pandita RK, Charaka VK, Hambarde S, et al. Pre-existing H4K16ac levels in euchromatin drive DNA repair by homologous recombination in S-phase. Commun Biol 2019;2:253 doi 10.1038/s42003-019-0498-z. [PubMed: 31286070]
59. Dow J, Krysztofiak A, Liu Y, Colon-Rios DA, Rogers FA, Glazer PM. Vulnerability of IDH1-Mutant Cancers to Histone Deacetylase Inhibition via Orthogonal Suppression of DNA Repair. Mol Cancer Res 2021;19(12):2057–67 doi 10.1158/1541-7786.MCR-21-0456. [PubMed: 34535560]
60. Sears TK, Horbinski CM, Woolard KD. IDH1 mutant glioma is preferentially sensitive to the HDAC inhibitor panobinostat. J Neurooncol 2021;154(2):159–70 doi 10.1007/s11060-021-03829-0. [PubMed: 34424450]
61. Xie S, Mortusewicz O, Ma HT, Herr P, Poon RY, Helleday T, et al. Timeless Interacts with PARP-1 to Promote Homologous Recombination Repair. Mol Cell 2015;60(1):163–76 doi 10.1016/j.molcel.2015.07.031. [PubMed: 26344098]
62. Young LM, Marzio A, Perez-Duran P, Reid DA, Meredith DN, Roberti D, et al. TIMELESS Forms a Complex with PARP1 Distinct from Its Complex with TIPIN and Plays a Role in the DNA Damage Response. Cell Rep 2015;13(3):451–9 doi 10.1016/j.celrep.2015.09.017. [PubMed: 26456830]
63. Rageul J, Park JJ, Zeng PP, Lee EA, Yang J, Hwang S, et al. SDE2 integrates into the TIMELESS-TIPIN complex to protect stalled replication forks. Nat Commun 2020;11(1):5495 doi 10.1038/s41467-020-19162-5. [PubMed: 33127907]
64. Leman AR, Noguchi C, Lee CY, Noguchi E. Human Timeless and Tipin stabilize replication forks and facilitate sister-chromatid cohesion. J Cell Sci 2010;123(Pt 5):660–70 doi 10.1242/jcs.057984. [PubMed: 20124417]
65. Bianco JN, Bergoglio V, Lin YL, Pillaire MJ, Schmitz AL, Gilhodes J, et al. Overexpression of Claspin and Timeless protects cancer cells from replication stress in a checkpoint-independent manner. Nat Commun 2019;10(1):910 doi 10.1038/s41467-019-08886-8. [PubMed: 30796221]
66. Wessel SR, Mohni KN, Luzwick JW, Dungrawala H, Cortez D. Functional Analysis of the Replication Fork Proteome Identifies BET Proteins as PCNA Regulators. Cell Rep 2019;28(13):3497–509 e4 doi 10.1016/j.celrep.2019.08.051. [PubMed: 31553917]
67. Bowry A, Piberger AL, Rojas P, Saponaro M, Petermann E. BET Inhibition Induces HEXIM1- and RAD51-Dependent Conflicts between Transcription and Replication. Cell Rep 2018;25(8):2061–9 e4 doi 10.1016/j.celrep.2018.10.079. [PubMed: 30463005]
68. Lam FC, Kong YW, Huang Q, Vu Han TL, Maffa AD, Kasper EM, et al. BRD4 prevents the accumulation of R-loops and protects against transcription-replication collision events and DNA damage. Nat Commun 2020;11(1):4083 doi 10.1038/s41467-020-17503-y. [PubMed: 32796829]

69. Chapuy B, McKeown MR, Lin CY, Monti S, Roemer MG, Qi J, et al. Discovery and characterization of super-enhancer-associated dependencies in diffuse large B cell lymphoma. Cancer Cell 2013;24(6):777–90 doi 10.1016/j.ccr.2013.11.003. [PubMed: 24332044]

70. Edwards DS, Maganti R, Tanksley JP, Luo J, Park JJH, Balkanska-Sinclair E, et al. BRD4 Prevents R-Loop Formation and Transcription-Replication Conflicts by Ensuring Efficient Transcription Elongation. Cell Rep 2020;32(12):108166 doi 10.1016/j.celrep.2020.108166. [PubMed: 32966794]

71. Lin CL, Tsai ML, Lin CY, Hsu KW, Hsieh WS, Chi WM, et al. HDAC1 and HDAC2 Double Knockout Triggers Cell Apoptosis in Advanced Thyroid Cancer. Int J Mol Sci 2019;20(2) doi 10.3390/ijms20020454.

72. Carrier F Chromatin Modulation by Histone Deacetylase Inhibitors: Impact on Cellular Sensitivity to Ionizing Radiation. Mol Cell Pharmacol 2013;5(1):51–9. [PubMed: 24648865]

73. Hazan I, Monin J, Bouwman BAM, Crosetto N, Aqeilan RI. Activation of Oncogenic Super-Enhancers Is Coupled with DNA Repair by RAD51. Cell Rep 2019;29(3):560–72 e4 doi 10.1016/j.celrep.2019.09.001. [PubMed: 31618627]

74. Caron MC, Sharma AK, O'Sullivan J, Myler LR, Ferreira MT, Rodrigue A, et al. Poly(ADP-ribose) polymerase-1 antagonizes DNA resection at double-strand breaks. Nat Commun 2019;10(1):2954 doi 10.1038/s41467-019-10741-9. [PubMed: 31273204]

75. Lu Y, Kwintkiewicz J, Liu Y, Tech K, Frady LN, Su YT, et al. Chemosensitivity of IDH1-Mutated Gliomas Due to an Impairment in PARP1-Mediated DNA Repair. Cancer Res 2017;77(7):1709–18 doi 10.1158/0008-5472.CAN-16-2773. [PubMed: 28202508]

76. Wang Y, Wild AT, Turcan S, Wu WH, Sigel C, Klimstra DS, et al. Targeting therapeutic vulnerabilities with PARP inhibition and radiation in IDH-mutant gliomas and cholangiocarcinomas. Sci Adv 2020;6(17):eaaz3221 doi 10.1126/sciadv.aaz3221. [PubMed: 32494639]

77. Vikas P, Borcherding N, Chennamadhavuni A, Garje R. Therapeutic Potential of Combining PARP Inhibitor and Immunotherapy in Solid Tumors. Front Oncol 2020;10:570 doi 10.3389/fonc.2020.00570. [PubMed: 32457830]

78. Jiao S, Xia W, Yamaguchi H, Wei Y, Chen MK, Hsu JM, et al. PARP Inhibitor Upregulates PD-L1 Expression and Enhances Cancer-Associated Immunosuppression. Clin Cancer Res 2017;23(14):3711–20 doi 10.1158/1078-0432.CCR-16-3215. [PubMed: 28167507]

79. Sim HW, Galanis E, Khasraw M. PARP Inhibitors in Glioma: A Review of Therapeutic Opportunities. Cancers (Basel) 2022;14(4) doi 10.3390/cancers14041003.

80. Ramos R, Climans SA, Adile A, Ghiassi P, Baker S, Phillips MJ, et al. Combination olaparib and durvalumab for patients with recurrent IDH-mutated gliomas. Journal of Clinical Oncology 2021;39(15_suppl):e14026–e doi 10.1200/JCO.2021.39.15_suppl.e14026.

Translational Relevance:

Our understanding of radioresistance mechanisms in patient-derived glioma cell cultures (GCC) that endogenously express mIDH1-R132H are limited. We have uncovered a novel gene target Zinc Finger MYND-Type Containing 8 (ZMYND8) that is downregulated following treatment of human mIDH1 GCCs with mIDH1 specific inhibitors. We demonstrate that suppression of ZMYND8 expression by shRNA knockdown or genetic knockout reduces the cellular viability of mIDH1 GCCs to ionizing radiation (IR). Our findings reveal an epigenetic vulnerability of mIDH1 GCCs to ZMYND8 knockout (KO) which results in impaired resolution of IR-induced DNA damage and induction of cell cycle arrest. Additionally, ZMYND8 KO mIDH1 GCCs display increased radiosensitivity to inhibition of epigenetic regulators BRD4, HDAC, and PARP which could be mediated by enhanced replicative stress.

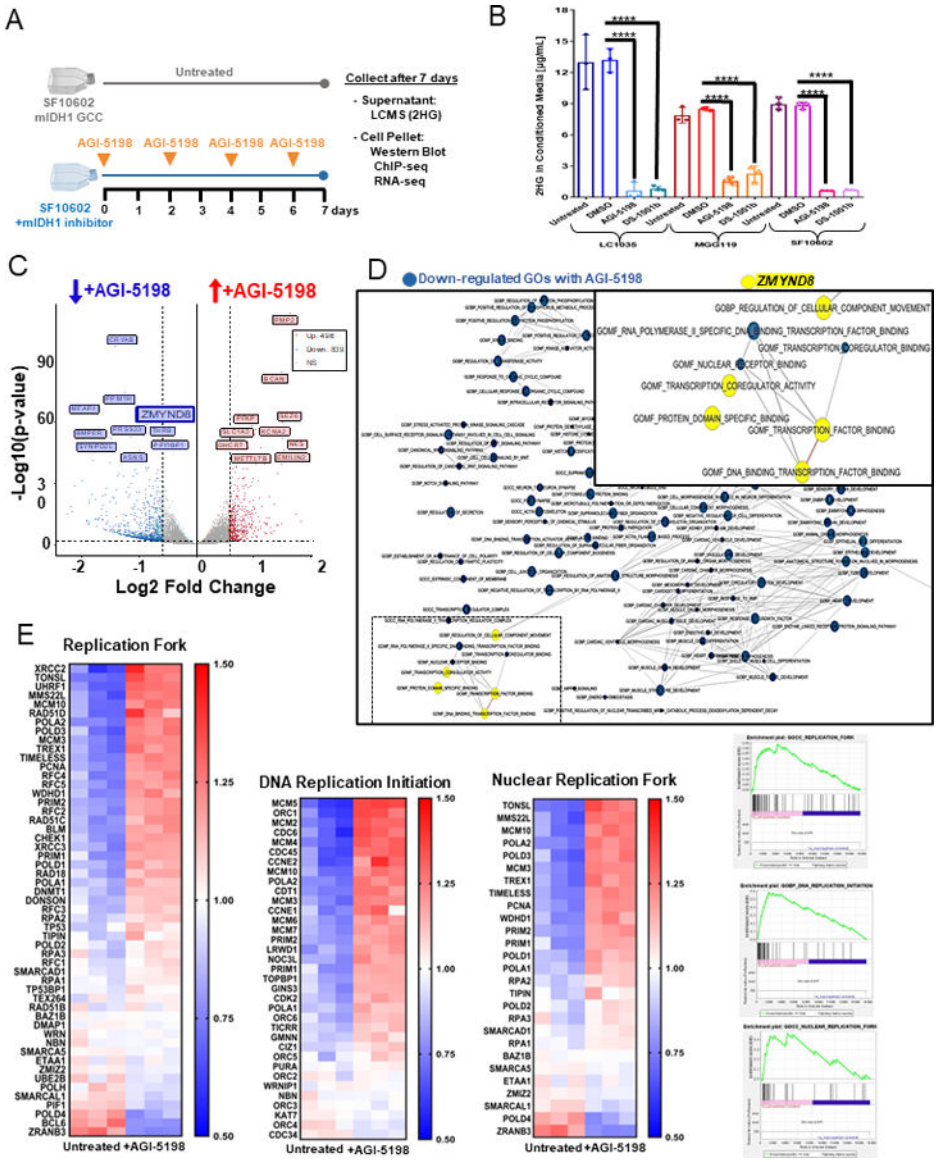

Figure 1: Inhibition of mIDH1-R132H in a patient-derived glioma cell culture (SF10602) leads to increased activation of DNA damage associated gene ontologies (GO).

(**A**) Experimental schematic of downstream analyses comparing untreated SF10602 human glioma cell culture (GCC) that endogenously express the R132H mutation in isocitrate dehydrogenase 1 (mIDH1) with cells treated with 5μM AGI-5198 (a mIDH1 specific inhibitor). After 1 week, the supernatant was collected for liquid chromatogram and mass spectrometry (LCMS) and cell pellet was utilized for transcriptomic (RNA-sequencing), epigenomic (ChIP-sequencing) and protein (Western blot) analysis. (**B**) Representative histogram displays the liquid chromatography and mass spectrometry (LC/MS) measurement in microgram per microliter (μg/mL) of 2-hydroxyglutarate (2HG), an oncometabolite produced by mIDH1, present within the conditioned media of three patient-derived mIDH1 GCCs [LC1035, MGG119 and SF10602]. Samples were collected from untreated, vehicle treated (DMSO), mIDH1 inhibitor (AGI-5198) or clinical mIDH1 inhibitor (DS-1001b). Errors bars represent standard error of mean (SEM) from independent

biological replicates (n=3). **** P < 0.0001; unpaired t test. (**C**) Volcano plot of differentially expressed genes (DEG) based on RNA-seq analysis comparing AGI-5198 treated SF10602 vs. untreated. Dots represent individual genes, genes found to be downregulated in AGI-5198 treated mIDH1 GCCs vs. untreated are shown in blue, up-regulated in red, or non-statistically significant (NS) difference in grey. (**D**) Gene Set Enrichment Analysis (GSEA) map of downregulated GOs following AGI-5198 treatment. The yellow highlighted nodes specify the GOs terms containing ZMYND8, which were associated with transcription factor binding and cellular movement. (**E**) Heatmap depicting the relevant GOs related to DNA replication initiation and replication forks that were upregulated in AGI-5198 treated GCCs compared to untreated. The corresponding GSEA enrichment plot is adjacent, where the green line represents the enrichment score for a given GO as the analysis proceeds along the rank list of DEG.

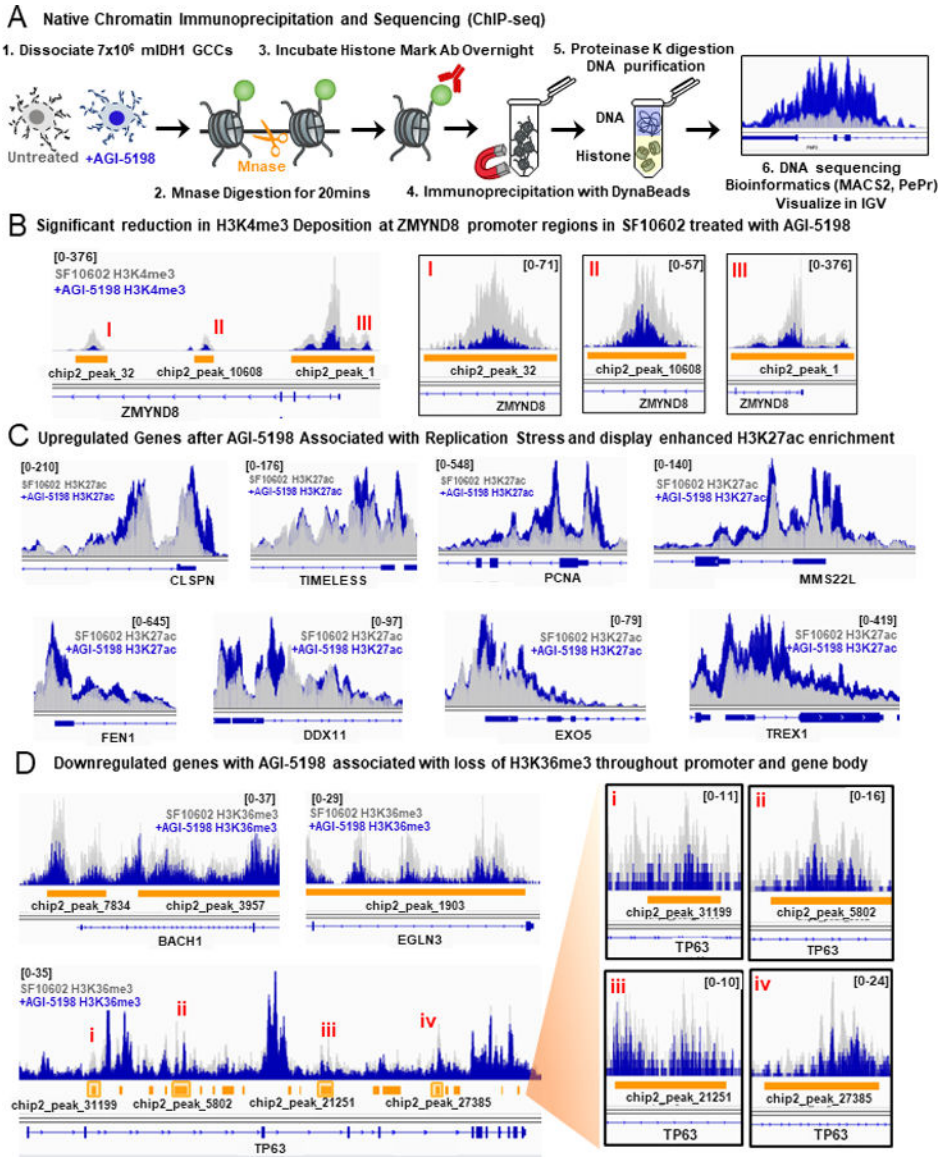

Figure 2: Epigenomic changes in histone mark deposition following mIDH1 inhibition.

(**A**) Diagram detailing the steps of native chromatin immunoprecipitation and sequencing (ChIP-seq) (**B**) Integrative Genomics Viewer (IGV) image displays overlapping tracks comparing the H3K4me3 occupancy in specific genomic regions near the ZMYND8 promoter in untreated SF10602 (grey, two replicates) and AGI-5198 treated (dark blue, two replicates). The y-axis represents the number of immunoprecipitated fragments for a given histone mark normalized to the total number of reads per sample and mapped to the human genome reference (hg19) along the x-axis. Regions that display significant changes in histone mark deposition based on peak-calling prioritization pipeline (PePr) comparison between untreated SF10602 vs. AGI-5198 treated SF10602 are represented by orange bars and the red roman numerals signify distinct regions that are expanded to the right. (**C**) IGV screenshots of H3K27ac deposition at the promoters of specific genes associated with replication stress. (**D**) IGV screenshots of H3K36me3 deposition throughout the promoter

and gene body, where select regions that lost H3K36me3 deposition by PePr calling at TP63 locus are indicated by yellow squares.

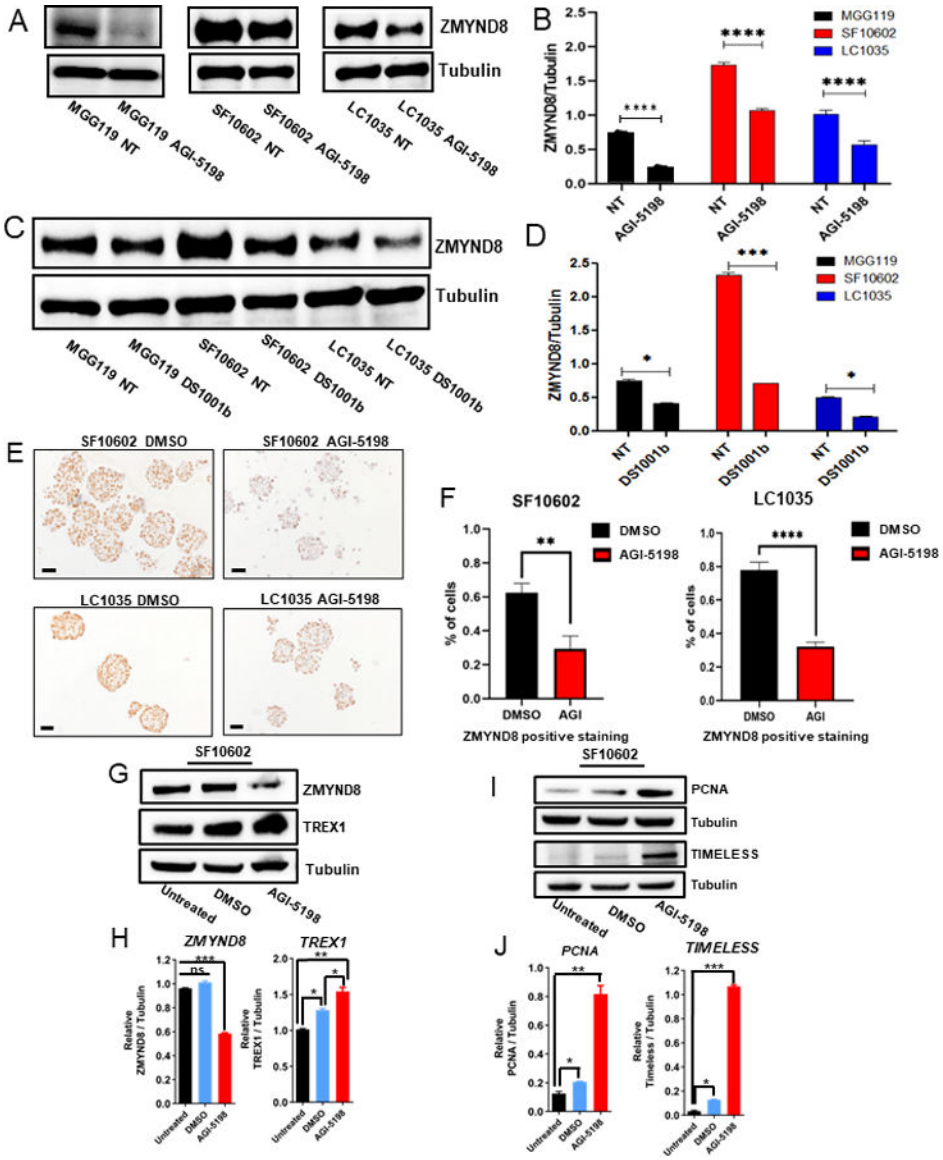

Figure 3: Decreased ZMYND8 protein expression following mIDH1 inhibitor treatment (AGI-5198, DS1001b) in mIDH1 GCCs, coincides with an increased expression of genes associated with genomic instability.

(**A**) Representative western blot for ZMYND8 protein expression in three human mIDH1 GCCs that were non-treated (NT) or AGI-5198-treated (mIDH1 inhibitor) for 1 week. (**B**) ImageJ densitometric quantification of ZMYND8 protein expression based relative to loading control (tubulin) for each of the mIDH1 GCCs either NT or AGI-5198 treated: MGG119 (black), SF10602 (red), and LC1035 (blue). (**C**) Representative western blot for ZMYND8 protein expression in three human mIDH1 GCCs that were NT or DS1001b treated (clinical mIDH1 inhibitor) for 1 week. (**D**) ImageJ densitometric quantification of ZMYND8 protein expression following DS1001b treatment compared to NT. (**E**) Immunohistochemistry (IHC) staining of sectioned paraffin-embedded human mIDH1 GCCs treated with vehicle (DMSO) or mIDH1 inhibitor (AGI-5198). (**F**) Representative Quantitative Pathology & Bioimage Analysis (QuPath) of IHC slides to identify the

percentage of ZMYND8 positive staining (Diaminobenzidine (DAB) optical density > 0.4) for 12 representative frames. (**G**) Western blot analysis shows ZMYND8 and TREX1 expression in SF10602 mIDH1 GCC either untreated, DMSO, or AGI-5198 treatment for 1 week with tubulin as a loading control. (**H**) ImageJ densitometric quantification of the western blot for ZMYND8 and TREX1. (**I**) Western blot analysis shows PCNA and TIMELESS expression in SF10602 either untreated, DMSO, or AGI-5198 treatment for 1 week with tubulin as a loading control. (**J**) ImageJ densitometric quantification of the western blot for PCNA and TIMELESS. Errors bars represent SEM from independent biological replicates (n=3). * P<0.05, ** P<0.01, *** P<0.001, **** P < 0.0001; unpaired t test

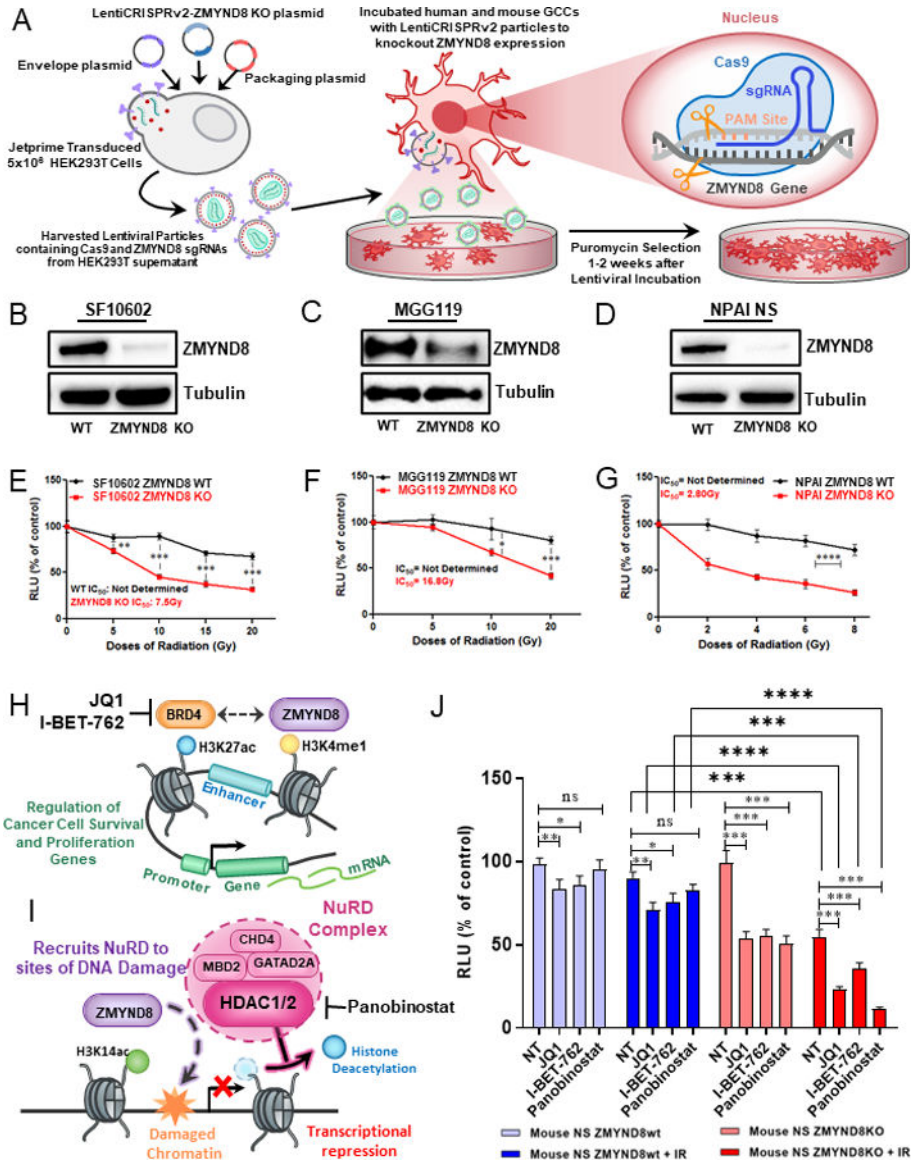

Figure 4: ZMYND8 Knockout GCCs display reduced viability to irradiation, which is further enhanced when combined with BRD4 and HDAC inhibition.

(**A**) Experimental model in which ZMYND8 lentiviral particles were generated to knockout (KO) ZMYND8 expression in human and mouse GCCs mediated by CRISPR-Cas9-sgRNAs. ZMYND8 KO GCCs were selected based on resistance to 10μg/mL puromycin for 1 week in mouse mIDH1 GCCs and 2 weeks for human mIDH1 GCCs. Representative western blot quantification of ZMYND8 KO for (**B**) SF10602, (**D**) MGG119 and (**F**) NPAI mouse NS. Cellular viability of ZMYND8 wildtype (WT, shown by black line) vs. ZMYND8 KO, represented by the red line, was assessed 72 hours after irradiation (IR) exposure using CellTiter-Glo assay in the (**C**) SF10602, (**E**) MGG119 and (**G**) NPAI. Results are expressed in relative luminescence units (RLU) to control non-irradiated (0 Gy) cells. (**H**) Working model of ZMYND8-interacting partner Bromodomain-containing protein (BRD4), where ZMYND8 is recruited to enhancer regions marked by H3K4me1 and contributes to the regulation of cancer cell survival and proliferation associated genes. BRD4

inhibitors, JQ1and I-BET-762, can disrupt this interaction. (**I**) Working model of ZMYND8-interacting partner HDAC1/2 (histone deacetylase 1/2); a component of the Nucleosome Remodeling and Histone Deacetylase (NuRD) complex, where ZMYND8 binds H3K14ac residues present at damaged chromatin regions and recruits HDAC along with other NuRD subunits: MDB2, CHD4, and GATAD2A. Panobinostat inhibits HDAC1/2 and prevents histone deacetylation mediated by HDAC1/2, which is required for transcriptional repression at regions of DNA damage. (**J**) Representative bar graph of cellular viability measured in RLU, which shows the effect of BRD4 (JQ1, I-BET-762) or HDAC (Panobinostat) inhibition alone (−IR) or in combination with irradiation (+IR) in mouse NPAI ZMYND8 wt in blue vs. NPAI ZMYND8 KO in red. Errors bars represent SEM from independent biological replicates (n=3). ns-not significant, * $P<0.05$, ** $P<0.01$, *** $P<0.001$, **** $P < 0.0001$; unpaired t test

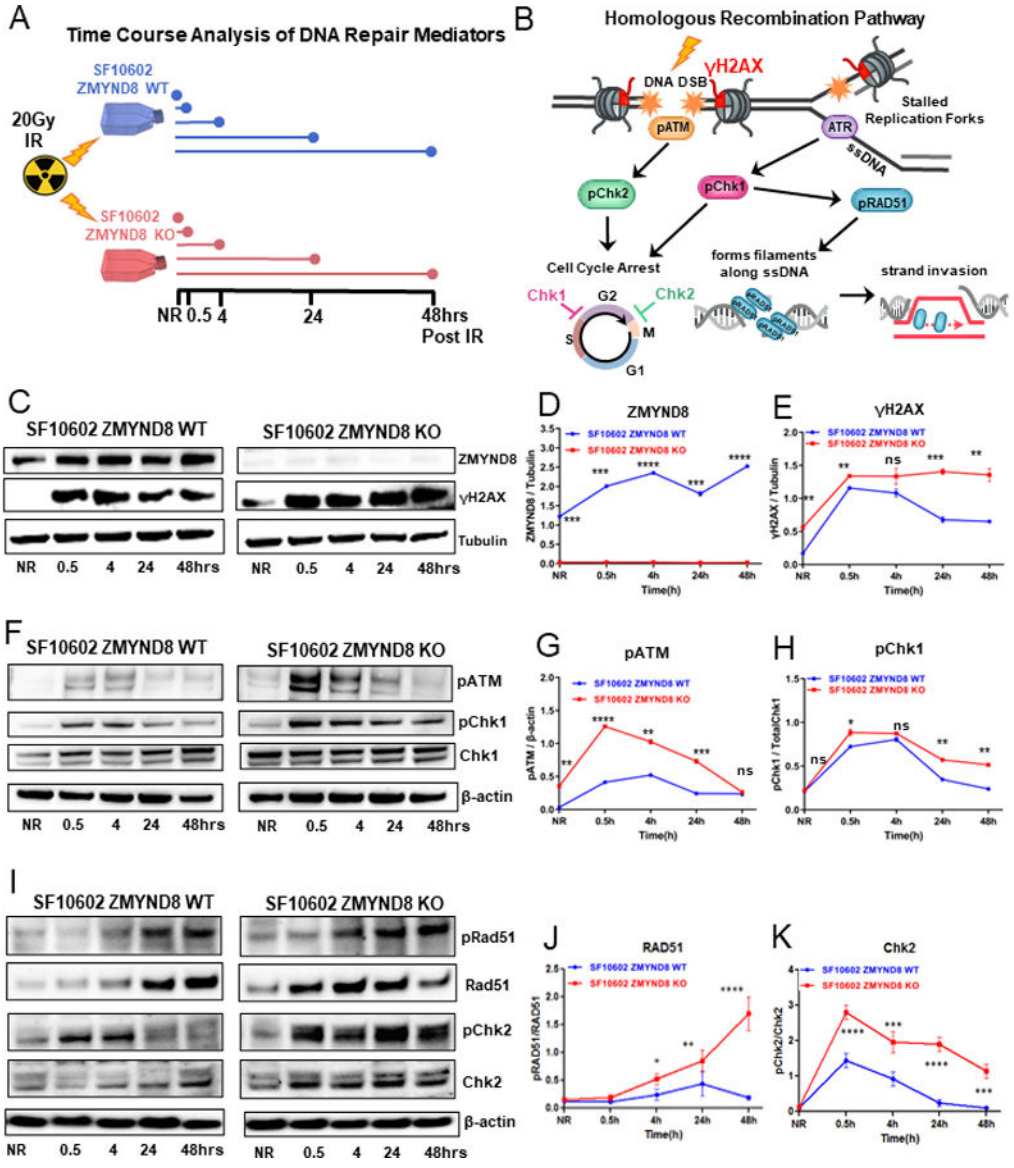

Figure 5: ZMYND8 KO mIDH1 GCCs are defective in resolving IR induced DNA damage and undergo prolonged activation of cell cycle arrest.

(A). Diagram of the time course analysis of DNA repair proteins expressed in SF10602 ZMYND8 WT (blue) vs. SF10602 ZMYND8 KO (red) exposed to a single dose of 20Gy IR and protein was collected from non-irradiated (NR) cells and at 0.5, 4, 24, and 48 hours post IR exposure. (**B**) Model of irradiation (lighting blot) induced activation of the homologous recombination (HR) pathway including downstream HR mediators. (**C**) Representative western blot for ZMYND8 and γH2AX expression in SF10602 ZMYND8 WT vs. SF10602 ZMYND8 KO at the indicated conditions described in IR time course diagram. (**D**) Line graph represents the quantification of ZMYND8 expression relative to tubulin in SF10602 ZMYND8 WT (blue) vs. SF10602 KO (red) from 0 (NR) to 48hrs post IR. (**E**) Line graph represents the quantification of γH2AX relative to tubulin. (**F**) Representative western blot for phosphorylated ATM (pATM) and Chk1 (pChk1) expression and their respective nonphosphorylated (ATM and Chk1) proteins relative to β-actin. Line

graph represents the quantification of (**G**) pATM expression relative to β-actin and (**H**) pChk1 expression relative to Chk1. (**I**) Representative western blot for phosphorylated Rad51 (pRad51) and Chk2 (pChk2) expression and their respective nonphosphorylated (Rad51 and Chk2) proteins relative to β-actin. Line graph represents the quantification of (**J**) pRad51 expression relative to Rad51 and (**H**) pChk2 expression relative to Chk2. Error bars represent SEM from independent biological replicates. (n=3) * P<0.05, ** P<0.01, *** P<0.001, **** P < 0.0001; unpaired t test.

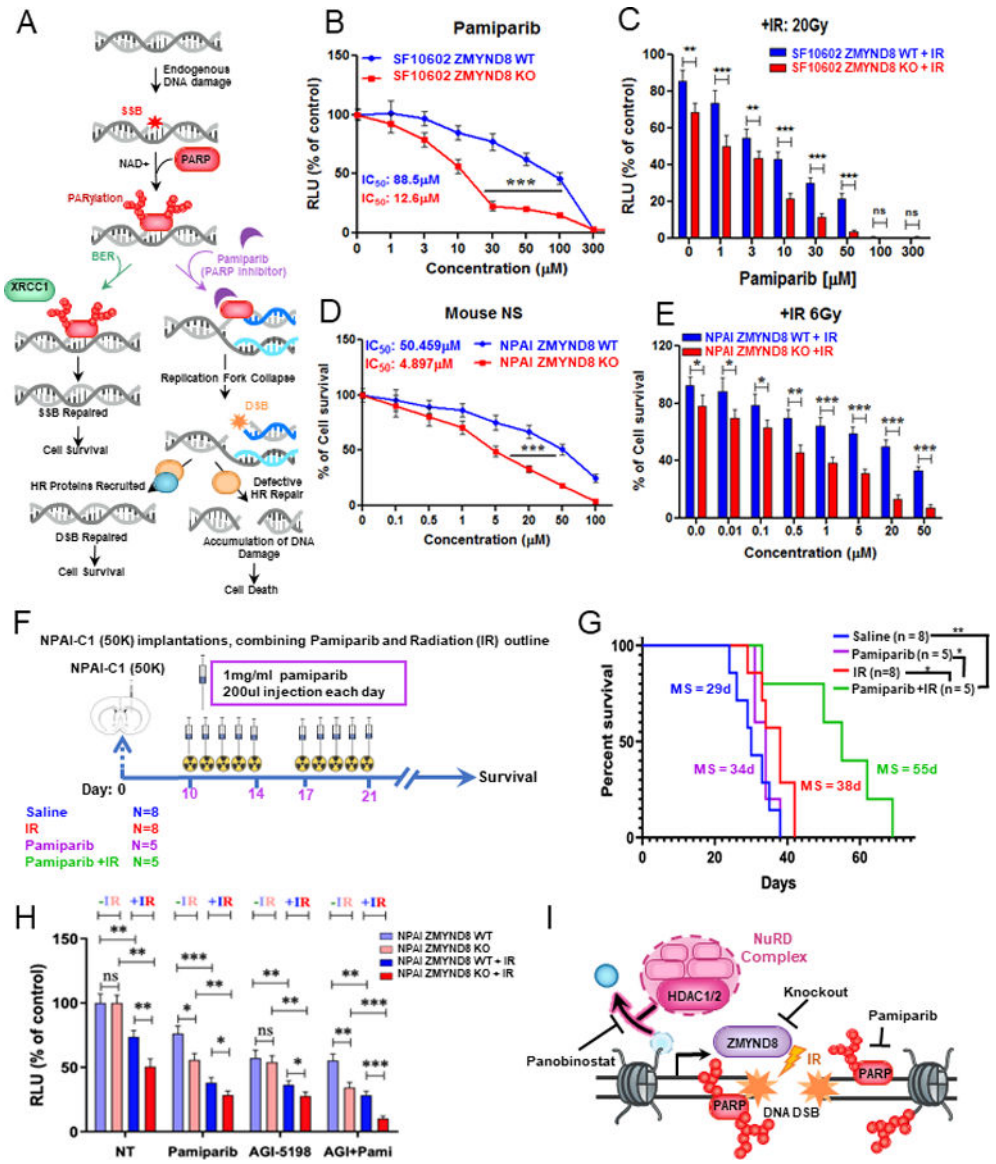

Figure 6: ZMYND8 KO mIDH1 GCCs are more susceptible to PARP inhibition.

(A) Proposed mechanism of PARP's repair of single stranded breaks (SSB), which occur as a results of endogenous DNA damage in proliferating cells. PARP1/2 catalyze a reaction that utilizes nicotinamide adenine dinucleotide (NAD+) to add poly(ADP-ribose) polymers to itself and signals the recruitment of proteins involved in base excision repair (BER) like XRCC1 to resolve the SSB. Pamiparib (PARP inhibitor) block PARPylation and trap PARP onto DNA, resulting in the formation of double stranded breaks (DSB) at collapsed replication forks. Cells that can successfully recruit HR proteins can repair the DSB. (**B**) Pamiparib dose response curve to evaluate the impact of PARP inhibition on SF10602 ZMYND8 WT (blue) vs. SF10602 ZMYND8 KO (red). Two-tailed t test. (**C**) Cell viability assay shows the effect of Pamiparib + Irradiation (IR 20Gy) on cell proliferation in SF10602 ZMYND8 WT vs. SF10602 ZMYND8 KO measured in RLU relative to control non-treated. Two-tailed t test. (**D**) Pamiparib dose response curve from mouse NPAI mIDH1 GCCs

ZMYND8 WT (blue) vs. NPAI ZMYND8 KO (red). Two-tailed t test. (**E**) Cell viability assay shows the effect of Pamiparib + IR 6Gy on cell proliferation in NPAI ZMYND8 WT (blue) vs. NPAI ZMYND8 KO (red) measured in RLU relative to control IR alone (0μM Pamiparib). Two-tailed t test. (**F**) Preclinical design for testing the impact of PARP inhibitor (Pamiparib) on the response to IR in an orthotopic glioma model. Ten days after implantation of 50,000 NPAI NS, animals were randomly divided into 4 groups: (i) saline, (ii) IR received 2Gy/day for 5 days each cycle (20Gy total) starting 10 days post implantation (dpi) (iii) Pamiparib delivered intraperitoneal (1mg/mL injection) 5 days on and 2 days off for 2 weeks, (iv) Pamiparib + IR. Mice were monitored for tumor burden and euthanized at symptomatic stages to track survival to treatment. (**G**) Kaplan-Meier survival curve of NPAI ZMYND8 WT tumor bearing mice treated with or without 6Gy (n=8) in the presence or absence of Pamiparib (n=5). $*P < 0.05$, $**P < 0.01$; log-rank Mantel-Cox test. (**H**) Impact of mIDH1 inhibition (AGI-5198) and Pamiparib alone or in combination on the cellular viability of NPAI ZMYND8 WT in the presence (+IR) or absence (−IR) of irradiation. Errors bars represent SEM from independent biological replicates (n=3). ns-not significant, * P<0.05, ** P<0.01, *** P<0.001, **** P < 0.0001; Multiple one-tail t test was used (**I**) Working model in which targeting ZMYND8 by genetic knockout or treatment with HDAC or PARP inhibition exposes an epigenetic vulnerability of mIDH1 GCCs to IR induced DNA damage.